Bulletin of Mathematical Biology (2007) 69: 1477–1510
DOI 10.1007/s11538-006-9172-y

ORIGINAL ARTICLE

Discrete Cilia Modelling with Singularity Distributions: Application to the Embryonic Node and the Airway Surface Liquid

D. J. Smith[a,b,c,*], E. A. Gaffney[a,1], J. R. Blake[a]

[a] *School of Mathematics, University of Birmingham, Birmingham B15 2TT, UK*
[b] *Reproductive Biology and Genetics, School of Medicine, University of Birmingham, Birmingham B15 2TT, UK*
[c] *Assisted Conception Unit, Birmingham Women's Hospital Trust, Birmingham B15 2TG, UK*

Received: 26 July 2006 / Accepted: 20 September 2006 / Published online: 1 May 2007
© Society for Mathematical Biology 2007

Abstract We discuss in detail techniques for modelling flows due to finite and infinite arrays of beating cilia. An efficient technique, based on concepts from previous 'singularity models' is described, that is accurate in both near and far-fields. Cilia are modelled as curved slender ellipsoidal bodies by distributing Stokeslet and potential source dipole singularities along their centrelines, leading to an integral equation that can be solved using a simple and efficient discretisation. The computed velocity on the cilium surface is found to compare favourably with the boundary condition. We then present results for two topics of current interest in biology. 1) We present the first theoretical results showing the mechanism by which rotating embryonic nodal cilia produce a leftward flow by a 'posterior tilt,' and track particle motion in an array of three simulated nodal cilia. We find that, contrary to recent suggestions, there is no continuous layer of negative fluid transport close to the ciliated boundary. The mean leftward particle transport is found to be just over 1 μm/s, within experimentally measured ranges. We also discuss the accuracy of models that represent the action of cilia by steady rotlet arrays, in particular, confirming the importance of image systems in the boundary in establishing the far-field fluid transport. Future modelling may lead to understanding of the mechanisms by which morphogen gradients or mechanosensing cilia convert a directional flow to asymmetric gene expression. 2) We develop a more complex and detailed model of flow patterns in the periciliary layer of the airway surface liquid. Our results confirm that shear flow of the mucous layer drives a significant

*Corresponding author.
E-mail addresses: D.J.Smith.2@bham.ac.uk (D. J. Smith), gaffney@maths.ox.ac.uk (E. A. Gaffney), J.R.Blake@bham.ac.uk (J. R. Blake).
[1] *Present address:* Centre for Mathematical Biology, Mathematical Institute, 24–29 St. Giles,' Oxford OX1 3LB, UK

volume of periciliary liquid in the direction of mucus transport even during the recovery stroke of the cilia. Finally, we discuss the advantages and disadvantages of the singularity technique and outline future theoretical and experimental developments required to apply this technique to various other biological problems, particularly in the reproductive system.

Keywords Singularity · Slender body theory · Embryonic nodal cilia · Airway surface liquid

1. Introduction—the modelling of cilia-driven flow by slender body theory

Cilia are microscopic hair-like appendages found throughout most of the animal kingdom in, among others, the digestive, excretory, respiratory and reproductive systems. Cilia, typically, have radius of around 0.1–0.2 μm and length of from around 2–3 μm for 'primary cilia' in the embryonic node to around 6 μm in the lungs and over 10 μm in microscopic swimming organisms. Cilia have the same internal structure as eukaryotic flagella such as the spermatozoon tail, which in some species can be over 100 μm in length.

Since cilia-driven flow velocities are typically of the order of less than 100 μm/s and oscillatory frequency less than 20 Hz, associated Reynolds numbers are typically no larger than 10^{-3} or 10^{-2}, even for fluid viscosities as low as water, and so the steady Stokes flow equations are employed. Cilia can be characterised as slender bodies, with slenderness ratio varying from 10 to over 100. A large body of techniques for modelling flows produced by individual or multiple slender bodies, exploiting the linearity of the Stokes flow equations has been developed, including the initial work of Burgers (1938), Hancock (1953) and Tuck (1964); techniques based on asymptotic expansions such as Batchelor (1970), Cox (1970), Tillett (1970) and the later, highly accurate work of Johnson (1980) and Bartha and Liron (1988a,b); slender bodies near or across fluid interfaces (Fulford and Blake, 1986a), models of arrays of cilia (Blake, 1972; Liron and Mochon, 1976a; Fulford and Blake, 1986b; Gueron and Liron, 1992); and models of flagellar propulsion Lighthill (1976); Higdon (1979). These techniques involve representing the action of a cilium by a centreline distribution of point forces, represented by the singular 'Stokeslet' solution, possibly together with higher order singularities such as the potential source dipole to satisfy the boundary condition on the surface of the flagellum. Additional recent developments include the development of a slender body method for unsteady Stokes flow by Clarke et al. (2006) to model high frequency microfluidics. These techniques are very desirable in that they reduce the solution of a three-dimensional PDE problem to the determination of a one-dimensional line of singularity strengths. They also take into account the moving boundary of the cilium surface in a very natural way, and allow for the inclusion of boundaries such as an epithelial surface or coverslip by the use of an appropriately chosen singularity (such as Blake, 1971; Liron and Mochon, 1976b).

In this paper, we shall describe a straightforward and efficient implementation of this technique for modelling the flow generated by multiple cilia with prescribed beat pattern. The technique combines the Chwang and Wu (1975) distribution

of Stokeslets and dipoles generating a slender ellipsoid, with variable Stokeslet strength to allow for a curved centreline, as in Johnson (1980), together with a simple integral equation algorithm that gives very acceptable results even in the near-field of the cilium. We apply the technique to two problems: the flow in the embryonic node, where a small number of primary cilia perform rotational motions about tilted axes to produce a directional flow; and the flow of periciliary liquid (PCL) in the liquid lining of the lung, using the metachronal simplification of Liron and Mochon (1976a) together with a combination of singularities that preserves both near and far-field accuracy while maintaining efficiency, and a physically based mucus velocity field as a boundary condition. Finally, we discuss future directions for singularity modelling in various biological systems.

2. Representing a single cilium

As in the work of Blake (1972) and Liron and Mochon (1976a), we begin by defining $\boldsymbol{\xi}(s,t)$, a curve describing the time-dependent shape of the centreline of a cilium whose base is fixed at the origin. $\boldsymbol{\xi}(s,t) = (\xi_1(s,t), \xi_2(s,t), \xi_3(s,t))$, where s is the arc length along the cilium, varying between 0 and L, and t is time, varying between 0 and T, where T is the period of the ciliary beat cycle. The ciliated surface lies in the plane $x_3 = 0$.

One could attempt to model the internal mechanics of the cilia in order to explore such questions as the emergence of the cilia/flagellar beat, or the emergence of metachronism: for example, see Gueron and Liron (1992, 1993); Gueron and Levit-Gurevich (2001). However, for this study, we shall focus on the flow fields produced by cilia with known beat pattern and frequency.

2.1. *Singularity solutions*

The Stokeslet $S_{jk}(\mathbf{x}, \mathbf{y})$ is the velocity at $\mathbf{x}$ due to a point force at $\mathbf{y}$ in the $\mathbf{e}_k$ direction, hence the vector $\mathbf{S}_k = (S_{1k}, S_{2k}, S_{3k})$ is the solution of the Stokes flow equations

$$\begin{aligned} -\nabla p_k + \mu \nabla^2 \mathbf{S}_k + \mathbf{e}_k \delta(\mathbf{x} - \mathbf{y}) = 0, \\ \nabla \cdot \mathbf{S}_k = 0, \end{aligned} \tag{1}$$

where δ denotes the three-dimensional Dirac delta distribution. The velocity field resulting from some point force $\mathbf{f}$ is then given by $\mathbf{u} = \mathbf{S}_k f_k$. Here and in what follows, we use the summation convention.

In an infinite fluid $S_{jk}^{\infty} = (\delta_{jk}/r + r_j r_k / r^3)/(8\pi\mu)$. The potential dipole, or doublet, is a higher order singularity given by $K_{jk} = (\delta_{jk}/r^3 - 3 r_j r_k / r^5)/(4\pi)$. This singularity decays much more rapidly, and will have a far less significant effect on the far-field when compared with the Stokeslet. However, in the near-field it may be important.

Cilia do not beat in an infinite volume, the dominant boundary effect being that of the surface they are attached to. Based on the observation that the curvature of such surfaces is generally small compared with the cilium length, the surface is

generally modelled as an infinite plane $x_3 = 0$. In order to model micro-organism swimming, Blake (1971) derived using Fourier transforms the image system for a point force in a semi-infinite region $x_3 > 0$ with a no-slip boundary at $x_3 = 0$. The semi-infinite singularity may be represented by the infinite domain Stokeslet, an equal and opposite image Stokeslet in the boundary, and a combination of the higher order singularities of the 'stresslet' and 'Stokes doublet' to give a far-field that, quite unlike the infinite domain solution, decays with $O(1/r^2)$. We shall use this solution in Section 3, in order to show how tilted rotating nodal cilia interact with a plane boundary to effect net propulsion. For reference, the explicit form of the solution is:

$$S_{jk}^{\infty/2} = \frac{1}{8\pi\mu}\left[\left(\frac{\delta_{jk}}{r} + \frac{r_j r_k}{r^3}\right) - \left(\frac{\delta_{jk}}{R} + \frac{R_j R_k}{R^3}\right) + 2y_3(\delta_{k\alpha}\delta_{\alpha l} - \delta_{k3}\delta_{3l})\frac{\partial}{\partial R_l}\left(\frac{y_3 R_j}{R^3} - \left(\frac{\delta_{j3}}{R} + \frac{R_j R_3}{R^3}\right)\right)\right], \tag{2}$$

where the distance to the image point $R = [R_1^2 + R_2^2 + R_3^2]^{1/2} = [(x_1 - y_1)^2 + (x_2 - y_2)^2 + (x_3 + y_3)^2]^{1/2}$.

To represent the flow in a region confined between two closely opposed surfaces, such as the periciliary region between the ciliated epithelium and the mucous layer, we will use the Stokeslet derived by Liron and Mochon (1976b) for a point force in the domain $-\infty < x_1 < \infty$, $-\infty < x_2 < \infty$ and $0 < x_3 < L$, as shown in Fig. 4. This solution was derived originally to model flow in ciliated reproductive tract. We shall use it to model flow in the periciliary layer, which has depth approximately equal to the cilia length L. In this paper, we denote it S_{jk}^C; we also consider the summed and integrated form of this, $D_{jk}^C(x_1, x_3, \xi_1, \xi_3) := \sum_{q=-\infty}^{\infty} \int_{-\infty}^{\infty} S_{jk}^C(x_1, x_2, x_3, \xi_1 + q\lambda, 0, \xi_3)\, \mathrm{d}x_2$ where λ is the metachronal wavelength defined in Section 4.1. In summary, we use the following singularities:

S_{jk}^{∞} Stokeslet for point force in the infinite domain,

$S_{jk}^{\infty/2}$ Stokeslet for point force in the semi-infinite domain $x_3 \geqslant 0$,

S_{jk}^{C} Stokeslet for point force in the confined domain $0 \leqslant x_3 \leqslant L$,

$$D_{jk}^{C} := \sum_{q=-\infty}^{\infty} \int_{-\infty}^{\infty} S_{jk}^{C}(x_1, x_2, x_3, \xi_1 + q\lambda, 0, \xi_3)\, \mathrm{d}x_2, \tag{3}$$

K_{jk} potential source dipole in the infinite domain

G_{jk}^{∞} infinite Stokeslet + dipole combination defined in Eq. (9),

G_{jk}^{C} confined domain Stokeslet + dipole combination.

2.2. *Using singularity distributions to represent the cilium*

Since the cilium is a slender body, we require that there will be an approximately constant velocity on any circular cross section. We also require that for any given motion of the cilium $\dot{\boldsymbol{\xi}}$, there exists a centreline distribution of singularities that will give rise to a fluid flow $\mathbf{u}$ that is equal to $\dot{\boldsymbol{\xi}}$ on the whole of the surface of the cilium. We compare three different distributions, to determine which gives the most satisfactory representation. To begin with, we will work in the infinite domain.

2.3. *Stokeslet distribution*

Slender body theories are based on the concept of replacing the cilium with a line distribution $\mathbf{S}_k^{\infty}(\mathbf{x}, \boldsymbol{\xi}(s,t))$, of strength $f_k(\boldsymbol{\xi}(s,t))$. With the summation convention, the velocity field given by a line of Stokeslets alone is

$$\mathbf{u}(\mathbf{x},t) = \int_0^L \mathbf{S}_k^{\infty}(\mathbf{x}, \boldsymbol{\xi}(s^*,t))\, f_k(\boldsymbol{\xi}(s^*,t))\, \mathrm{d}s^*. \tag{4}$$

Applying this equation on the cilium, $\mathbf{u}(\boldsymbol{\xi}(s,t)) = \dot{\boldsymbol{\xi}}(s,t)$ and so

$$\dot{\boldsymbol{\xi}}(s,t) = \int_0^L \mathbf{S}_k^{\infty}(\boldsymbol{\xi}(s,t), \boldsymbol{\xi}(s^*,t))\, f_k(\boldsymbol{\xi}(s^*,t))\, \mathrm{d}s^*. \tag{5}$$

Hence we have a Fredholm integral equation of the first kind for the force distribution $f_k(\boldsymbol{\xi}(s,t))$. In what follows, we nondimensionalise with L as the length scale, σL at the velocity scale, σ^{-1} as the time scale and $\mu\sigma L^2$ as the force scale (so that the scaling for f_k is $\mu\sigma L$). The singularity $\mathbf{S}_k$ is, therefore, rescaled with respect to $(\mu L)^{-1}$. Since the problem has no t dependence, the solution at any point in time depends only on $\boldsymbol{\xi}$ and $\dot{\boldsymbol{\xi}}$ at that time. Consequently, throughout much of this study, it will be convenient to take t to be fixed and suppress the t dependence.

2.4. *Discretisation*

One could solve this equation by directly replacing the integral with a quadrature formula and solve the resulting matrix equation. However, $\mathbf{S}_k^{\infty}(\mathbf{x}, \boldsymbol{\xi})$ varies very rapidly for $\mathbf{x}$ close to $\boldsymbol{\xi}$, so that the calculated velocity on the surface exhibits unacceptable oscillations between meshpoints. Hence, we divide the cilium into the segments $((i-1)/N, i/N)$ with midpoints $s_i = (i-0.5)/N$, and assume that the force distribution $f_k(\boldsymbol{\xi}(s))$ can be approximated by the midpoint value $f_k(\boldsymbol{\xi}(s_i))$. This leads to

$$\begin{aligned}\dot{\boldsymbol{\xi}}(s_q) = &\sum_{i=1, i\neq q}^{N} f_k(\boldsymbol{\xi}(s_i)) \int_{(i-1)/N}^{i/N} \mathbf{S}_k^{\infty}(\boldsymbol{\xi}(s_q), \boldsymbol{\xi}(s^*))\, \mathrm{d}s^* \\ &+ f_k(\boldsymbol{\xi}(s_q)) \int_{(q-1)/N}^{q/N} \mathbf{S}_k^{\infty}(\boldsymbol{\xi}(s_q) + \alpha\mathbf{n}, \boldsymbol{\xi}(s^*))\, \mathrm{d}s^*,\end{aligned} \tag{6}$$

where $\mathbf{n} = (n_1, 0, n_3)$ is the normal to the cilium axis in the plane in which the cilia beat. We can then apply the midpoint rule with Q points to each integral, using the midpoints $s_{il} = (i-1)/N + (l-0.5)/(QN)$. Hence, we have

$$\dot{\boldsymbol{\xi}}(s_q) = \frac{1}{QN}\left(\sum_{i=1, i\neq}^{N}\sum_{l=1}^{Q}\mathbf{S}_k^{\infty}(\boldsymbol{\xi}(s_q), \boldsymbol{\xi}(s_{il}))\, f_k(\boldsymbol{\xi}(s_i)) + \sum_{l=1}^{Q}\mathbf{S}_k^{\infty}(\boldsymbol{\xi}(s_q) + \alpha\mathbf{n}, \boldsymbol{\xi}(s_{ql}))\, f_k(\boldsymbol{\xi}(s_q))\right). \tag{7}$$

This is essentially the algorithm used by Liron and Mochon (1976a), but with additional refinement to prevent oscillations between meshpoints. The $+\alpha\mathbf{n}$ term moves the point of evaluation off the cilium axis and onto a point on its surface to ensure that the Stokeslet is large, but finite. We shall verify that the boundary conditions are satisfied to a high degree of accuracy *a posteriori*.

Equation (8) can be rearranged into a system of $3N$ equations for $3N$ unknowns, the $f_k(\boldsymbol{\xi}(s_i))$ for $i = 1, \ldots, N$ and $k = 1, 2, 3$, and solved numerically, for example, with the F04AAF NAG library routine. The solution for the velocity field may then be calculated using the discretised version of Eq. (4). The above discretisation technique will be used for all subsequent integral equations in this paper.

When solving integral equations of the first kind, various difficulties may be encountered. One such problem is the existence of non-trivial solutions f to the homogeneous equation $0 = \int_0^1 f(s)S(s)\,\mathrm{d}s$—this means that the inhomogeneous problem will not have a unique solution and numerical results may be incorrect. We have tested the algorithm with $\dot{\boldsymbol{\xi}}$ set to zero, but the only solution obtained for f was the zero solution. It is important when discretising this type of integral equation that the resulting matrix is not singular or severely ill-conditioned, otherwise the solution is likely to be wildly oscillating. The kernel S_{jk}^{∞} becomes large at points where $r = n$, which is useful because it ensures the diagonal elements of the matrix are relatively large compared with the other elements, so that the solution is stable.

Once the force distribution is found, the algorithm can be checked for consistency by evaluating the velocity on the cilium surface. Using $\mathbf{n} = (n_1, 0, n_3)$ and $\mathbf{b} = (0, 1, 0)$ to denote the unit normal and binormal to the cilium centreline, we apply two tests: is the velocity on the line $\boldsymbol{\xi}(s) + \alpha\mathbf{n}$ on the cilium surface equal to the cilium velocity $\partial\boldsymbol{\xi}/\partial t(s, t)$, and is the velocity constant on the circle $\boldsymbol{\xi}(s) + \alpha\cos\theta\mathbf{n} + \alpha\sin\theta\mathbf{b}$, on the cilium surface for $0 < \theta < 2\pi$?

Numerical results for this algorithm are shown in Fig. 1. In graph (A), there is an excellent fit to the boundary conditions except for near the cilium tip, where the calculated velocity diverges significantly from the cilium velocity. Graph (B) shows a variation of around 10% in the velocity moving around the cylinder. We now consider refined approaches that represent the cilium more accurately.

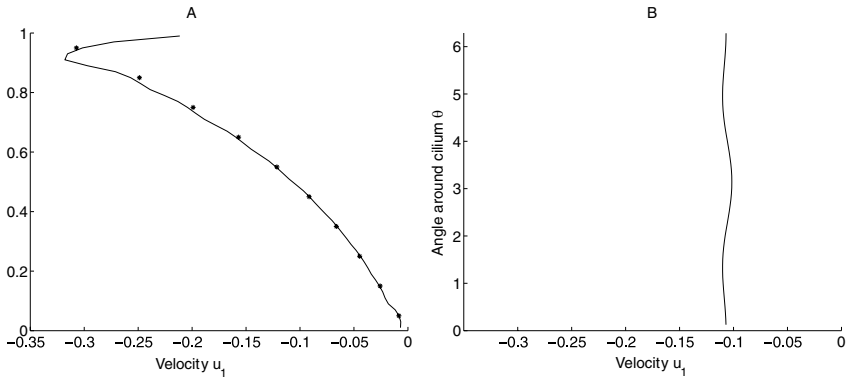


Fig. 1 (A) Profile along cilium for Stokeslet code, true cilium velocity at node points given by *. $N = 10$, $Q = 11$, $\alpha = 0.1/6$. (B) Profile around cilium at $s = 0.5$.

2.5. Adding the potential source dipole to improve accuracy

The initial work of Burgers (1938) and Hancock (1953) was developed by Tuck (1964), Cox (1970), Batchelor (1970), Tillett (1970) and others using the theory of matched asymptotics. Slender bodies of various cross sections and in various incident flows were still represented by line distributions of Stokeslets, but with the force distributions being determined by asymptotic theory. Expansions were taken in the parameter $(\log \epsilon)^{-1}$, where ϵ is the slenderness ratio, which is not ideal due to it not being a particularly small parameter. Inspired by a Hancock's original study, Lighthill (1976) suggested that flagella could better be modelled by considering the combined action of Stokeslets and potential dipoles distributed on their axes. As proved in Childress (1981), the flow at $x = 0$ around a straight circular cylinder of radius a, lying on the x–axis between $x = -b$ and $x = c$ ($a, b, c > 0, a \ll b, c$) is given by a distribution of Stokeslets of strength $\mathbf{f}$ and dipoles of strength $a^2\mathbf{f}^n/4\mu$, where $\mathbf{f}^n$ is the component of $\mathbf{f}$ normal to the cilium axis. A corresponding 'curved cylinder' shape at an instant during the beat cycle is shown in Fig. 2(A).

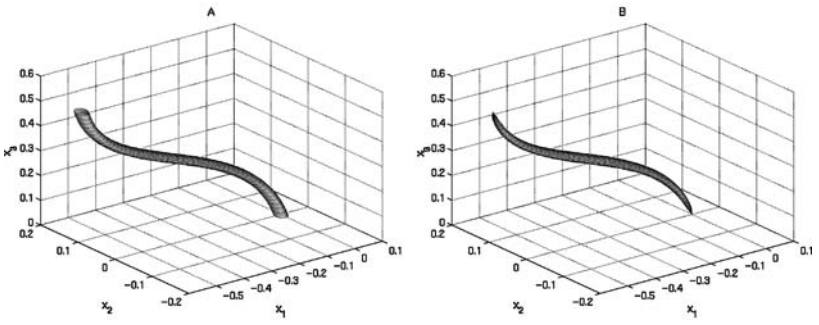


Fig. 2 (A) Cylindrical cilium. (B) Ellipsoidal cilium.

Lighthill presented a result that was remarkably simple and elegant. The flow due to a combination of Stokeslets and dipoles representing a cylinder '... is closely matched by flagellar motions such that the cross section of a flagellum at s_0 moves with velocity

$$\frac{\mathbf{f}_n(s_0)}{4\pi\mu} + \int_{r_0 > \frac{1}{2}a\sqrt{\epsilon}} \mathbf{f} \cdot \left[\frac{\underline{\mathbf{I}}}{8\pi\mu r_0} + \frac{\mathbf{r}_0\mathbf{r}_0}{8\pi\mu r_0^3} \right] \mathrm{d}s \ldots' \tag{8}$$

The first term is the normal force on the flagellum, the second term is a non-singular line integral of Stokeslets. The error was found by Childress (1981) to be $O(\epsilon^{1/2})$, errors in the velocity on the surface of the cylinder due to centreline curvature κ and variation in the force distribution f were shown by Lighthill to be $O(a\kappa)$ and $O(af\,\mathrm{d}f/\mathrm{d}s)$, respectively. This 'Lighthill theorem' was extended further to model cilia by Gueron and Liron (1992) to include the effect of a nearby boundary, and to extract a term in the tangential component of the force also, since this term may, in fact, be dominant. This technique, known as the 'LGL theorem' is particularly efficient due to the fact that it requires only the evaluation of a non-singular integral. It is very suitable for more computationally difficult problems such as the emergence of a coordinated beat, as, for example, the recent study of Gueron and Levit-Gurevich (2001). A slightly different approach employed by Higdon (1979) in modelling bacterial swimming was to retain the full Stokeslet and dipole distribution but integrate the singular parts analytically and use numerical integration for the regular parts. This was later found to compare very favourably with results using the much more computationally expensive Boundary Integral Equation method (Phan-Thien et al., 1987).

However, as noted by Liron (2001), this 'cylinder' representation has the limitation that it is not accurate near the ends of the cilium, particularly the distal end. This may be expected, since Batchelor (1970) noted that, '... for a body as far from being longitudinally elliptic as is a cylinder, the numerical accuracy of the [Stokeslet distribution] is rather limited unless [the slenderness ratio] is exceeding large...'

An alternative approach is to model the cilium as a curved slender ellipsoid, as depicted in Fig. 2(B). Chwang and Wu (1975) showed that the flow around a straight prolate spheroid $x^2/\beta^2 + (y^2+z^2)/\alpha^2 = 1$, $\beta \geq \alpha$ is given precisely by a distribution of Stokeslets with strength $\mathbf{f}$ and dipoles with strength $(l^2 - x^2)\alpha^2/2\beta^2\mathbf{f}$. The focal length is $2l$, so that $l = (\beta^2 - \alpha^2)^{1/2}$. In nondimensional units, where the cilium length is 1, we choose $l = 1/2$, then $\beta^2 = 1/4 + \alpha^2$. For this study, we shall use the values $\alpha = 0.1/3, 0.1/6$, which give $\beta = 0.5011, 0.5003$. Chwang and Wu (1975) calculated the force for a straight ellipsoid in a number of incident flows explicitly, but, for flexibility, we shall fix only the ratio of Stokeslet and dipole strengths, and revert to the numerical approach to determining the force distribution. This has much in common with the leading order solution technique of Johnson (1980), although he derived a second-kind integral equation to be solved iteratively, whereas we shall determine the force distribution directly.

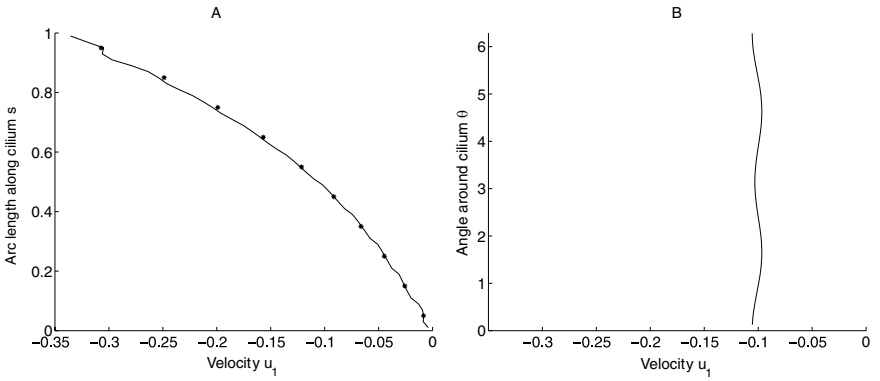


Fig. 3 (A) Profile along cilium for slender ellipsoid representation. $N = 10$, $Q = 11$, $\alpha = 0.1/6$. (B) Profile around cilium at $s = 0.5$.

Hence, we replace the singularity distribution in Eq. (4) with

$$\mathbf{G}_k^{\infty}(\mathbf{x}, \boldsymbol{\xi}(s^*)) := \mathbf{S}_k^{\infty}(\mathbf{x}, \boldsymbol{\xi}(s^*)) + \frac{\alpha^2}{1/2 + 2\alpha^2} s^*(1 - s^*)\mathbf{K}_k(\mathbf{x}, \boldsymbol{\xi}(s^*)). \tag{9}$$

In what follows, the presentation is much simplified by using the operator notation:

$$\mathbf{I}[\mathbf{x}, \boldsymbol{\xi}; \underline{\mathbf{G}}^{\infty}, \mathbf{f}] := \int_0^1 \mathbf{G}_k^{\infty}(\mathbf{x}, \boldsymbol{\xi}(s^*))\, f_k(\boldsymbol{\xi}(s^*))\, \mathrm{d}s^*, \tag{10}$$

to write the resulting integral equation in the simple form,

$$\dot{\boldsymbol{\xi}}(s) = \mathbf{I}[\boldsymbol{\xi}(s), \boldsymbol{\xi}; \underline{\mathbf{G}}^{\infty}, \mathbf{f}], \quad (0 < s < 1). \tag{11}$$

In Fig. 3(A) there is a very significant improvement in the fit between the cilium velocity and the calculated velocity at the cilium tip. Figure 3(B) shows that the variations in velocity around the cilium are still very small, comparable with the results for the Stokeslet and cylinder algorithm.

2.6. Singularity distributions for the semi-infinite and confined domain

The above models were designed for a slender body moving in an infinite domain. However, in order to model a cilium in a semi-infinite region ($x_3 > 0$) or a confined region ($0 < x_3 < L$) such as the oviduct or periciliary layer, we employ the semi-infinite Stokeslet that satisfies $S_{jk}^{\infty/2}(x_3 = 0) = 0$ and the confined domain Stokeslet, that additionally satisfies $S_{jk}^{C}(x_3 = 0) = 0 = S_{jk}^{C}(x_3 = L)$, as depicted in Fig. 4. We shall not modify the dipole, due to its higher-order decay. It is necessary to verify that the ellipsoid representation given above is still accurate. Simulation results are given in Figs. 5 and 6. The profile along the length of the cilium is again very satisfactory, even at the tip. The relative error in the velocity on a

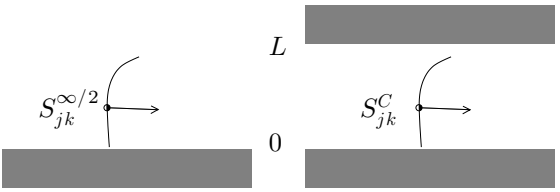


Fig. 4 *Left*—the semi-infinite domain $x_3 > 0$. *Right*—the confined domain $0 < x_3 < L$.

circle around the cilium is less than 0.1, which is very acceptably accurate. It may be noted that due to the dipole not being zero at the no-slip boundary $x_3 = 0$, there is a small deviation from the expected smooth convergence to zero velocity. However, the error is still very small in relation to the bulk of the fluid flow, and, in particular, any error will decay away from the cilium with $O(1/r^3)$, and so will not significantly affect conclusions for the flow in most of the liquid. Based on the calculations presented here, we conclude that the slender ellipsoid is the best representation for the cilium, and will use this in the rest of the study.

In the next section, we apply the technique to a simple system that captures some of the important physics of flow generation by a small number of embryonic nodal cilia, in order to show the physical mechanism by which a directional flow is established. Then, in Section 4, we present a more detailed model for flow in the airway surface liquid of the lungs than has previously been considered. This demonstrates how the discrete cilia approach can be used to obtain a high level of detail regarding a system that has already been extensively studied.

3. Flow generation by embryonic nodal cilia

Cilia-driven flows have been implicated in establishing left/right symmetry breaking in mouse embryo development (see, for example Nonaka et al., 2005), and a nodal flow has been observed in a number of species (see, for example Okada

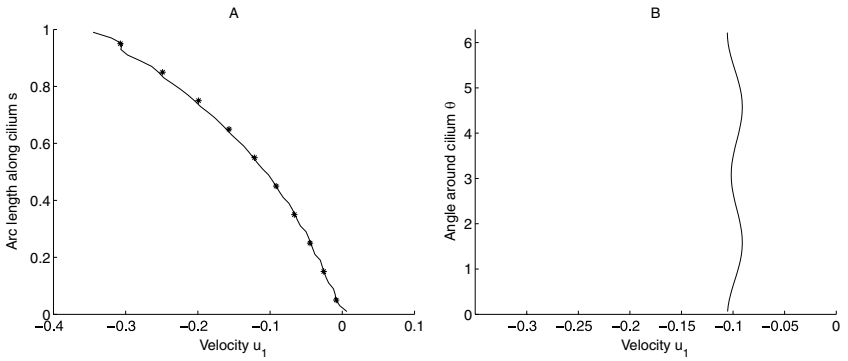


Fig. 5 (A) Profile along cilium for slender ellipsoid algorithm, semi-infinite domain. $N = 10$, $Q = 11$, $\alpha = 0.1/6$. (B) Profile around cilium at $s = 0.5$.

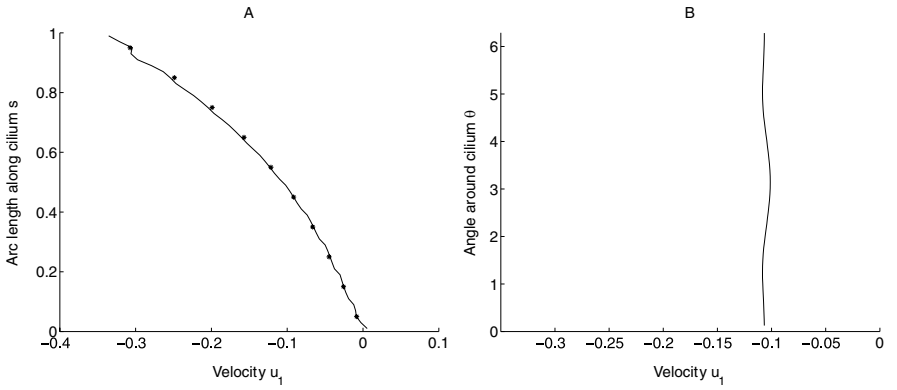


Fig. 6 (A) Profile along cilium for slender ellipsoid algorithm, confined domain. $N = 10$, $Q = 11$, $\alpha = 0.1/6$. (B) profile around cilium at $s = 0.5$.

et al., 2005). At around 8 days post-fertilization, following the establishment of the anteroposterior and dorsal–ventral axes, a structure known as the ventral node is observed on which are found primary cilia. These cilia have size around 2–3 μm and they rotate with an approximate frequency of 10 Hz about an axis tilted towards the posterior (Okada et al., 2005). The degree of tilt may be less, as indicated by the measurements of Nonaka et al. (2005) who found an average tilt that has recently been measured as being approximately 40° (Okada et al., 2005), but other results suggest it may be less (Nonaka et al., 2005). The node has a roughly triangular shape, is around 50 μm across and is covered by Reichert's membrane (Nonaka et al., 1998). The cavity is filled with extraembryonic liquid, and has a depth of the order of 20 μm (based on the data of Okada et al., 2005). Nodal cilia have been found to transport debris and tracer particles to the 'left' of the node in a plane close to the ciliated surface, with a corresponding 'rightward' counterflow occurring above due to the space being sealed. Furthermore, a mechanical model of cilia at low Reynolds number has been shown to replicate this effect (Nonaka et al., 2005). For consistency with the biological literature, the axes are designated as in Fig. 7. Note that in our results in Figs. 9–13, the positive x_1 direction is the 'left' of the node, the negative the 'right.'

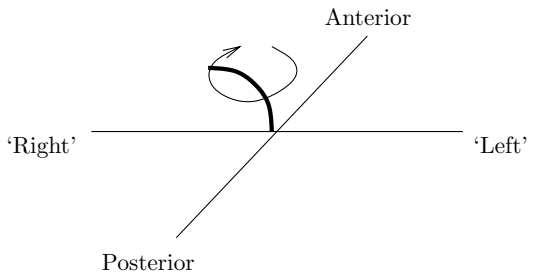


Fig. 7 The designation of the *left–right* and *anteroposterior* axes, and the clockwise rotation.

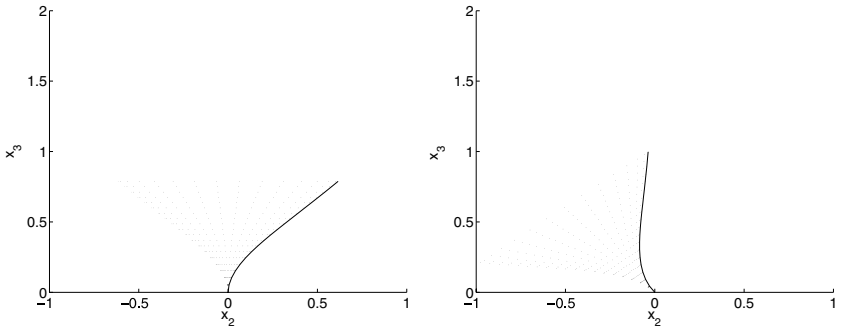


Fig. 8 Side view of the rotating cilium centreline shape. *Left*—without posterior tilt. *Right*—with posterior tilt of 40°. Note that the cilium is close to the boundary during the 'rightward' part of the rotation and further from the boundary during the 'leftward' part.

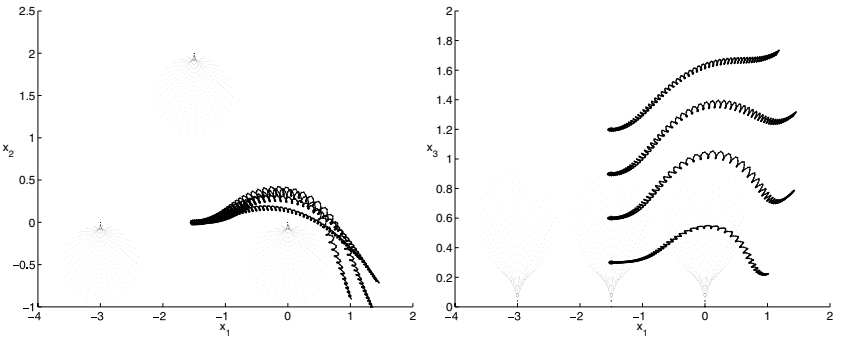


Fig. 9 Particle transport to the 'left' by three in-phase posterior-tilted clockwise rotating nodal cilia: initial particle positions are $(-1.5, 0, z)$, where $z = 0.3, 0.6, 0.9, 1.2$. Axes scaled with respect to cilium length 3 μm. Cilium radius is 0.1 μm. Time duration is 60 periods/6 s. There is no continuous layer of 'rightward' transport, since even the particle closest to the boundary $x_3 = 0$ is transported to the 'left.' Note that in this and all following results, the 'left' of the embryo is the positive x_1 direction, the *right* side of the graph.

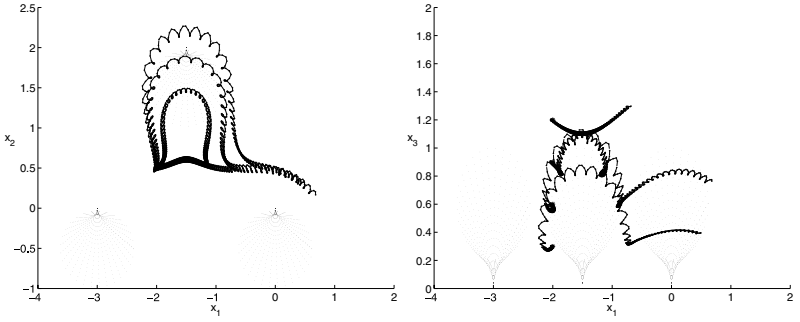


Fig. 10 Particle transport to the 'left' by three in-phase posterior-tilted clockwise rotating nodal cilia: initial particle positions are $(-2, 0.5, z)$, where $z = 0.3, 0.6, 0.9, 1.2$. Axes scaled with respect to cilium length 3 μm. Cilium radius is 0.1 μm. Time duration is 60 periods/6 s.

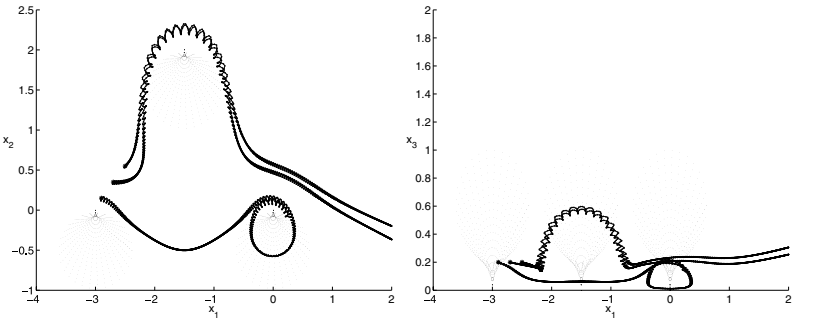


Fig. 11 Particle transport to the 'left' by three in-phase posterior-tilted clockwise rotating nodal cilia: Initial particle positions are $(-2.9, 0.15, 0.2)$, $(-2.7, 0.35, 0.2)$ and $(-2.5, 0.55, 0.2)$. Axes scaled with respect to cilium length $3\,\mu$m. Cilium radius is $0.1\,\mu$m. Time duration is 240 periods/24 s.

Recent data (Okada et al., 2005) suggest that the leftward flow in the mouse has velocity approximately 1–3 μm/s. Artifically reversing the flow reverses *situs* in the resulting embryo (Nonaka et al., 2002), so that, for example, the heart develops on the right rather than the left side. Mutant mouse embryos without cilia develop with random placement of internal organs (Nonaka et al., 1998), and humans with immotile cilia syndrome, which is associated with defective cilia often have *situs inversus* (Kosaki and Casey, 1998). The 'nodal flow' has, therefore, been implicated

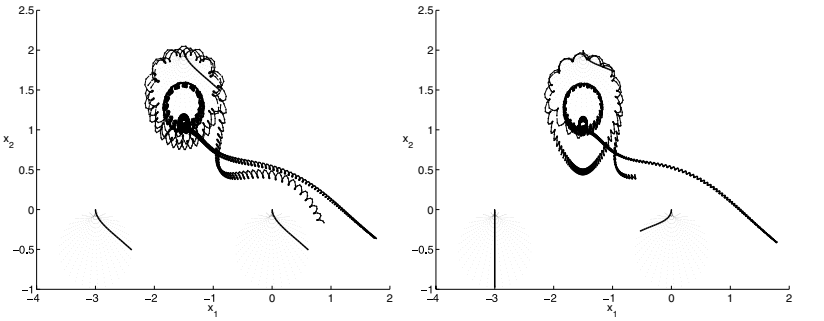


Fig. 12 Particle trapping and escape; the effect of phase difference: initial particle positions are $(-1.5, 1, z)$, where $z = 0.3, 0.6, 0.9, 1.2$. There is a vortex region that traps the particles starting at $z = 0.3, 0.6$ in approximately circular paths. The particle starting at $z = 0.9$ makes one or two complete circuits of the cilium before escaping, whereupon another cilium draws it to the 'left.' Compare with the 'circling and escape' behaviour observed by Nonaka et al. (1998). The particle starting at $z = 1.2$ above the cilium tip is immediately transported to the 'left'—it is not drawn into any rotational path. In the *left-hand* graph, the cilia are in phase, and the particle starting at $z = 0.9$ makes two complete circuits before escaping the cilium. In the *right-hand* graph, the cilia are out of phase, with initial positions of the cilia being shown by the continuous lines. The particle starting at $z = 0.9$ now follows a slower and more elongated path. On the second circuit, it escapes via a similar trajectory. Also, note that the particle starting at $z = 1.2$ moves a very similar distance for both arrays, suggesting that phase difference may not be a critical determinant of efficient transport. Axes scaled with respect to cilium length $3\,\mu$m. Cilium radius is $0.1\,\mu$m. Time duration is 90 periods/9 s.

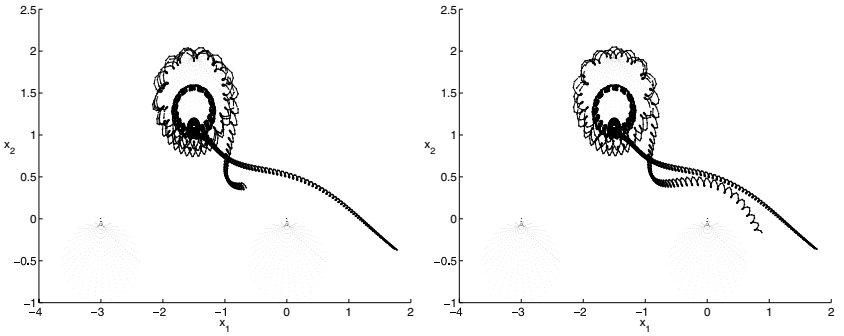


Fig. 13 The effect of the cilium length scale: for particles close to the envelope of a cilium, a small change to the cilium length scale while keeping the cilium radius constant can have a significant effect on particle pathlines. Initial particle positions are $(-1.5, 1, z)$, where $z = 0.3, 0.6, 0.9, 1.2$. *Left*—the cilium length scale is adjusted to $L = 2.95\,\mu$m, while the radius is kept constant at $0.1\,\mu$m. *Right*—for comparison, the pathlines with $L = 3\,\mu$m. For the relatively shorter cilia, the particle at $z = 0.9$ escapes more quickly. Axes scaled with respect to cilium length 2.95 and $3\,\mu$m, respectively. Cilium radius is $0.1\,\mu$m. Time duration is 90 periods/9 s.

in symmetry-breaking, but it is still not understood how the flow is produced mechanically, with existing publications (Cartwright et al., 2004; Buceta et al., 2005) either neglecting the boundary effect or altering the diameter of the cilium during the 'effective' and 'recovery' strokes. Furthermore, it is not understood how the flow is converted to asymmetric gene expression (McGrath et al., 2003). The original hypothesis (Nonaka et al., 1998) concerns the asymmetric distribution of morphogen chemicals, which may have 'inactivation times' (Cartwright et al., 2004) to prevent a uniform distribution occurring. Another hypothesis (Tabin and Vogan, 2003) states that sensory immotile cilia on opposite sides of the node bend differently in response to the flow, changing intracellular calcium ion levels differently. A detailed appreciation of the generation and of the oscillatory nature of the flow field would be of great assistance in determining how likely a chemical gradient is to be established, and parameters for inactivation times. It would also assist in determining how cilia on different sides of the node might be differently affected by the flow field.

Nodal cilia are much sparser than the dense cilia of the airways, as can be seen from the micrographs in Nonaka et al. (1998)—only one cilium protrudes from each cell. The spacing of the cilia is of the order of several cilium lengths. In addition to this, the ciliary beat is very different, being a tilted rotational motion rather than asymmetric shaped 'effective' and 'recovery' stroke as observed in standard '9 + 2' cilia (Sanderson and Sleigh, 1981). Brokaw (2005) and Nonaka et al. (2005) have noted that, much like the mechanism of standard ciliary propulsion (Blake and Sleigh, 1974), the interaction of the cilium with the nearby boundary during the rightward part of the stroke will limit the negative flow generated and, hence, result in a net leftward flow.

The purpose of this section is to demonstrate the utility of the discrete cilia technique and to explore the nature of the directional flow generated by a small array of tilted slender bodies through interaction with a plane boundary. In particular,

we shall be concerned with finding if there is a continuous rightward transport close to the boundary, as discussed by Nonaka et al. (2005). At this stage we shall not attempt a full model of the fluid dynamics in the node, and coupling the flow with symmetry breaking mechanisms, although these shall be subjects for future work.

In order to demonstrate the principles at work, we shall represent the cilium shape by the curve shown in Fig. 8. The positive and negative x_2 directions will be the 'anterior' and 'posterior' directions, respectively, so that the cilia are be tilted towards the negative x_2 direction. Viewed from above, the rotation will be clockwise. The ciliated surface will be given by $x_3 = 0$, and the fluid will be taken to occupy the domain $x_3 > 0$. This is a simplification of the real node that will have additional boundaries at the top and sides, but, at this stage, we will only be concerned with showing how the interaction with the nearby boundary causes a directional flow.

A finite array of m_0 cilia with known shape $\boldsymbol{\xi}^n$ and velocity $\dot{\boldsymbol{\xi}}^n$ $(n = 0, \ldots, m_0 - 1)$ can be represented using the above technique in a similar way to Eq. (11), only with the sum

$$\mathbf{u}(\mathbf{x}) = \sum_{r=0}^{m_0-1} \mathbf{I}[\mathbf{x}, \boldsymbol{\xi}^r; \underline{\mathbf{G}}, \mathbf{f}], \quad (0 < s < 1, n = 0, \ldots, m_0 - 1). \tag{12}$$

The resulting integral equation is then simply,

$$\dot{\boldsymbol{\xi}}^n(s) = \sum_{r=0}^{m_0-1} \mathbf{I}[\boldsymbol{\xi}^n(s), \boldsymbol{\xi}^r; \underline{\mathbf{G}}, \mathbf{f}], \quad (0 < s < 1, n = 0, \ldots, m_0 - 1). \tag{13}$$

Similar to the above, this discretises resulting in $3m_0N$ linear equations for the three scalar values of $\mathbf{f}$ at the N interpolation points on each of the m_0 cilia.

To determine the effect of the cilia on particles in the liquid, we used the following pathline tracking algorithm based on Heun's second-order ODE method:

time step i, position $\mathbf{x}_i$, time t_i
  calculate force distribution $\mathbf{f}(\boldsymbol{\xi}^r)$ at time t_i from $\boldsymbol{\xi}^r, \dot{\boldsymbol{\xi}}^r$ from Eq. (13)
  calculate velocity field $\mathbf{u}(\mathbf{x}_i, t_i)$ from Eq. (12)
  set $\mathbf{x}_i^* = \mathbf{x}_i + (\Delta t)\mathbf{u}(\mathbf{x}_i, t_i)$
  calculate force distribution $\mathbf{f}(\boldsymbol{\xi}^r)$ at time t_{i+1} from $\boldsymbol{\xi}^r, \dot{\boldsymbol{\xi}}^r$ from Eq. (13)
  calculate velocity field $\mathbf{u}(\mathbf{x}_i^*, t_{i+1})$ from Eq. (12)
  set $\mathbf{x}_{i+1} = \mathbf{x}_i + (\Delta t)(\mathbf{u}(\mathbf{x}_i, t_i) + \mathbf{u}(\mathbf{x}_i^*, t_{i+1}))/2$
go to time step $i + 1$ (14)

This algorithm demonstrates the utility of the singularity method: there is no need to calculate the flow over the whole domain at every timestep, it is simply enough

to find the strength of the force distributions and calculate the fluid velocity on the particle being tracked. Moreover, from the assumption of periodicity, it is only necessary to calculate the force distributions over one period of rotation.

To simulate dispersion of morphogen chemicals in the node, the effect of Brownian motion must be considered. For chemicals or tracer particles with a diffusion coefficient of less than 100 $\mu m^2/s$, the Peclet number will be less than 1, and hence Brownian motion will not be a dominant effect. For chemicals with higher diffusivities, a combined advection–diffusion formulation would be required. In the next section, we present results examining particle transport in the advective regime only.

3.1. Results

The results of tracking particles propelled by an array of three nodal cilia are given in Figs. 9–13. Except where stated, all the cilia are in phase, i.e. have equal phase angle, and rotate clockwise when viewed from above, with frequency 10 Hz. The axes labels are scaled with respect to cilium length L. Based on typical values of cilium length 3 μm and radius 0.1 μm, the parameter α is therefore 0.1/3. This parameter affects the force distribution and, hence, the flow field via Eq. (7). In all of the graphs, we shall refer to the positive x_1 direction as the 'left' of the node, which appears as the right-hand side of the diagrams.

Figure 9 shows how particles beginning in the centre of the array are swept to the 'left.' The net propulsion effect is very similar from $z = 0.3$ to $z = 1.2$, with all four particles drifting a similar distance. It is clear that there is no continuous layer of 'rightward' transport, even close to the floor of the node, which Nonaka et al. (2005) noted would be a consequence of the analysis of Cartwright et al. (2004). Note that the particle transport is relatively slow, in that it requires 60 cilium revolutions (6 s) to advect the particles just over 2 cilium lengths (6 μm). The speed of the leftward flow in the mouse appears to be 1–3 μm/s from the data of Okada et al. (2005). Hence, our simplified model gives results that are within the experimentally measured range.

Figure 10 shows pathlines for particles starting nearer to a cilium envelope. The particles starting from $z = 0.3$–0.9 are all drawn into a path around the nearby cilium. They are lifted above their starting locations by the tilted rotational velocity field, then swept back down to a symmetric position on the other side of the cilium and finally are drawn on to the 'left' by the combined far-field flow of all three cilia. In the absence of the nearby boundary, the particles would instead continue to circle the rotating cilium, but as noted by Brokaw (2005), due to the presence of a boundary, the flow generated by the leftward cilia movement is stronger than the flow generated by the rightward movement. Hence, the particles are swept to the 'left.' An alternative perspective is to consider the image system of a rotational flow in the wall, as discussed in Section 3.2.

Figure 11 shows three nearby particles starting close to the 'nodal floor' at $z = 0.2$. The particle starting closest to a cilium envelope is drawn even closer to the nodal floor, then travels very slowly (taking 200 revolutions or 20 s) across to an adjacent cilium, whereupon it is follows a circular path in which it may remain trapped for some time. The remaining two particles are drawn towards a different

cilium that lifts them above the surface, as in Fig. 10. The particles are then transported to the 'left,' finally exhibiting a gradual upward drift. This also corresponds to the stresslet far-field discussed in Section 3.2

It is also clear from Fig. 11 that relatively small changes to the initial position will at some points result in entirely different particle pathlines—possibly resulting in trapping by a cilium for one or many rotations, or transport directly to the 'left.'

Figure 12 shows the trapping and release of particles by a cilium 'vortex.' Particles starting at $z = 0.3$ and $z = 0.6$ are trapped in approximately circular paths, as would be predicted from the infinite rotlet model of Cartwright et al. (2004). The particle starting above the cilium tip at $z = 1.2$ is advected to the 'left,' and is drawn towards another cilium, although it does not enter its circulatory vortex. The particle starting at $z = 0.9$ behaves differently depending on the phase difference of the cilia (Fig. 12) or the cilium radius (Fig. 13). It performs one or several revolutions of the cilium before escaping to the 'left,' as observed by Nonaka et al. (1998). Conversely, phase difference does not appear to affect the main 'leftward' flow significantly.

3.2. Discussion

The particle tracking results show clearly how the posterior tilt interacts with the lower boundary to produce net 'leftward' transport. For particles starting sufficiently far from the envelopes of the cilia, they are generally advected to the 'left' no matter how close they are to the lower boundary. Particles between $x_3 = 0.3$ and $x_3 = 1.2$ are advected with speed approximately 1 μm/s, which is at the lower end of the range observed by Okada et al. (2005). Near the envelope of a cilium, particles starting near the level of the cilium tip are swept to the left, particles starting lower down may be trapped in vortical motion around the axis of rotation of the cilium. Our results are consistent with the video recordings of Okada et al. (2005) which show that just above the tips of the cilia, at around $x_3 = 4$ μm, there is continuous particle transport to the left. We also observed that particles closer to the envelope of a cilium may make one or several revolutions before being swept onwards to another cilium, as observed by Nonaka et al. (1998).

Cartwright et al. (2004) stated that '... corresponding to the directional flow above the rotlets, an equal and opposite flow exists below them. We should expect this counterflow in the node also, except that there it will be modified by the presence of the node walls ....' From the discrete cilia simulations, we do not observe a rightward flow close to the boundary, nor would we expect one since the boundary effect completely dominates any flow due to the rightward stroke of the cilium. Particles close to the path of the cilium may remain trapped in circular paths, but particles which are not trapped are always transported to the 'left.'

Close to the cilia envelopes, we observed that there may be chaotic dynamics, with particles which start close together following very different trajectories. We also found that particles will follow unpredictable 'circling and escape' trajectories that were sensitive to the radius to cilium length ratio, and the cilia phase difference. We did not undertake a study of measures of possible chaotic dynamics, but such mixing may have important implications for the establishment or smoothing

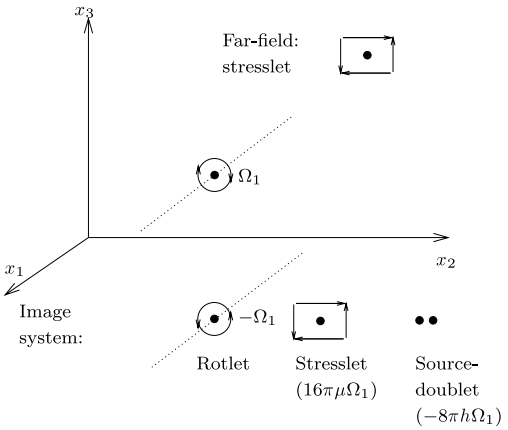


Fig. 14 The image system for a rotlet of strength Ω_1 with axis parallel to and a distance h from a plane boundary in Stokes flow is given by: an equal and opposite rotlet, a potential source doublet and a stresslet. In the far-field, the stresslet is dominant, which results in the net 'leftward' and 'lifting' particle paths evident in Fig. 13. Redrawn from Blake and Chwang (1974).

of chemical gradients. See, for example, Orme et al. (2001), which may be associated with symmetry-breaking mechanisms.

There are two ways to explain the generation of the nodal flow. As noted by Brokaw (2005), and used in the phenomenological model of Buceta et al. (2005), we can consider the tilted rotation as consisting of an 'effective' and a 'recovery' stroke as in '$9+2$' ciliary propulsion, which differ in propulsive effect due to the fact that the 'recovery' stroke takes place close to the boundary. An alternative perspective is to consider a steady rotlet representation, as used by Cartwright et al. (2004), but include the image systems associated with the plane boundary, as found by Blake and Chwang (1974) and shown in Fig. 14. Close to the axis of rotation, the particle paths resemble those around an infinite rotlet singularity, being approximately circular. In the far-field, the dominant singularity is the 'stresslet,' which pushes fluid 'left' and 'up,' i.e. in the positive x_1 and x_3 directions on the left of the node. This can be seen in the discrete cilia results of Fig. 11 for the two particles that escaped the array. With the appropriate image system, the rotlet representation may be very useful in investigating the dynamics of fluid transport in the node. A steady representation suppresses the effect of cilia phase difference, but this does not significantly affect the transport of the particles that are not trapped in a vortex. Phase difference or 'metachronism' (discussed for lung cilia in the next section) is likely not a critical determinant of flow generation for the more widely-spaced cilia of the embryonic node.

It should be noted that although the cilium tip moves faster than $100\,\mu$m/s, the bulk of the nodal flow is approximately 1–3 μm/s. This is because of the rapid decay of the stresslet velocity field, which is $O(1/r^2)$ due to the presence of the boundary. Because of this fast decay, cilia phase difference does not affect the majority of particles, and so we suggest it is unlikely that any interaction or mechanically induced metachronism could take place in the node.

Future modelling will take into account the upper boundary of the nodal cavity, although this is around 20 μm away and so will not have a dominant effect on the flow near the cilia (see Williams, 1966, where it is shown that the effect decays with $1/r$), and the walls of the cavity. Accurate experimental data on cilia movement (see, for example Nonaka et al., 2005) may also be included. In the longer term, determining the response of mechanosensory cilia or morphogen chemicals to this fluid flow may be possible, which will help to determine which mechanisms may be responsible for converting the fluid flow to asymmetric gene expression. Investigation of possible chaotic regions may also be useful in determining the nature of chemical advection–diffusion (Tang and Boozer, 1996).

A question that we have not explored is the origin of the clockwise rotation. Before the discovery of the nodal flow, Brown and Wolpert (1990) discussed the question of how molecular asymmetry could be converted to cellular asymmetry. They suggested that handedness of certain cellular structures, including the microtubules that comprise primary cilia, may be involved in converting antero–posterior and dorsal–ventral asymmetry to a cellular level. By modelling the internal force generation of the axoneme and coupling with a fluid mechanical model for interaction with the surrounding liquid, Brokaw (2005) has investigated mechanisms that may be responsible for the emergence of the chirality of cilium rotation, and the stability of the resulting chirality. The structural asymmetry of the axoneme, with dynein arms reaching in a clockwise direction from each tubule doublet was found not to be sufficient to establish chirality. Rather, other physical mechanisms such as clockwise microtubule rotation or control of dynein activity by sliding velocity of an adjacent doublet were found to be plausible. Coupling this modelling framework with consideration of the boundary effect, via the techniques described here is possible, and would provide a platform for the modelling of the interaction between cilia, the boundary and the flow field, in particular, possible response of mechanosensory cilia that may transduce the directional flow field.

4. Airway surface liquid transport by cilia

A topic of recent interest (Matsui et al., 1998; Smith et al., 2007) is the periciliary liquid (PCL) transport in the airway surface liquid layer of the lung. In the following sections, we derive a detailed model of the flow patterns in the periciliary layer that refines a previous model (Smith et al., 2006) of muco-ciliary transport.

4.1. The metachronal wave

We assume antiplectic metachronism, that is the metachronal wavefront propagates in the negative x_1–direction, the overlying mucus being transported in the positive x_1–direction. With this assumption, a cilium whose base is fixed at $x_1 = x$ will be described by $(x, 0, 0) + \boldsymbol{\xi}(s, kx/\sigma + t)$, $0 < s < 1$, where k is the wavenumber $2\pi/\lambda$, $\sigma/2\pi$ is the frequency and $c = \sigma/k$ is the wavespeed. The plus sign before the t indicates antiplectic metachronism. If we assume that the cilia have a

spacing a in the x_1–direction and b in the x_2–direction then the cilium at $(ma, nb, 0)$ is described by

$$\boldsymbol{\xi}'_{mn}(s,t) = (ma + \xi_1(s,\tau_m), nb + \xi_2(s,\tau_m), \xi_3(s,\tau_m)) \tag{15}$$

where

$$\tau_m = kma/\sigma + t, \qquad m, n = 0, \pm 1, \pm 2, \ldots \tag{16}$$

Blake (1973); Fulford and Blake (1986b); Liron and Mochon (1976a) and Liron (1978) all modelled the cilia as line distributions of Stokeslets $\mathbf{S}_k$ only, whereas in later sections we shall use the Stokeslet-dipole representation given by Eq. (9) in the near field.

Summing over the doubly infinite array of cilia represented by Stokeslet distributions, we have Eq. (11),

$$\mathbf{u}(\mathbf{x},t) = \sum_{n=-\infty}^{\infty}\sum_{m=-\infty}^{\infty}\int_0^1 f_k(\boldsymbol{\xi}'_{mn}(s^*,t))\mathbf{S}_k(\mathbf{x},\boldsymbol{\xi}'_{mn}(s^*,t))\,\mathrm{d}s^*. \tag{17}$$

It is not possible to solve the integral equation immediately, but there are various ways to rearrange it into a more tractable form.

An elegant approach used by Blake (1972) and Liron and Mochon (1976a) is to make use of the periodicity of the cilia beat cycle and synchronisation in the x_2 direction. After some manipulation, we have

$$\mathbf{u}(\mathbf{x},t) = \sum_{r=0}^{m_0-1}\int_0^1 f_k(\boldsymbol{\xi}^r(s^*,t))\sum_{q=-\infty}^{\infty}\sum_{n=-\infty}^{\infty}\mathbf{S}_k(\mathbf{x},\boldsymbol{\xi}'_{qm_0+r,n}(s^*,t))\,\mathrm{d}s^*, \tag{18}$$

where there are m_0 cilia per wavelength, and $\boldsymbol{\xi}^r(s^*,t) = \boldsymbol{\xi}(s^*, kra/\sigma + t)$. Blake (1972) now exploited the Poisson summation formula to convert the double sum into an exponentially decreasing series in the Fourier transformed Stokeslet. For many problems, this is a very useful approach because finding the singular solution for a particular domain involves first finding the Fourier-transformed version. Indeed, it may not in practice be possible to invert the transform. Possible applications of this might be the modelling of anisotropic liquids or porous media.

Instead of using the Poisson summation formula, Liron and Mochon (1976a) averaged the velocity and the sum of singularities in the x_2 direction. Due to synchronisation of the cilia in the x_2 direction, we have, in the notation of Eq. (10) the velocity $\bar{\mathbf{u}}(\mathbf{x})$ averaged in the x_2 direction:

$$\bar{\mathbf{u}}(\mathbf{x}) = \frac{1}{b}\sum_{r=0}^{m_0-1}\mathbf{I}[\mathbf{x} - ra\hat{\mathbf{x}}_1, \boldsymbol{\xi}^r; \underline{\mathbf{D}}, \mathbf{f}], \tag{19}$$

where

$$\underline{\mathbf{D}}(\mathbf{x}, \boldsymbol{\xi}) = \sum_{q=-\infty}^{\infty} \int_{-\infty}^{\infty} \underline{\mathbf{S}}(\mathbf{x} - \lambda q \hat{\mathbf{x}}_1, \boldsymbol{\xi})\, \mathrm{d}x_2. \tag{20}$$

Note that we have again suppressed the dependence on t—due to the assumption of metachronism, calculating the velocity field for one instant means that we automatically have the velocity field for times $t \pm r\,T/m_0$ for $r = \pm 1, 2, \ldots$ The kernel $\underline{\mathbf{D}}$ must be calculated for the appropriate domain from $\underline{\mathbf{S}}$, as for the semi-infinite domain in Liron and Mochon (1976a) and the confined domain in Liron (1978).

4.2. Pressure gradient

Liron (1978) observed that, due to the periodic boundary conditions in his problem, the solution was non-unique—an arbitrary constant pressure gradient could be added. As discussed in Smith et al. (2007), a subject of great interest is the transport of PCL in cultures that exhibit circular mucus transport, as described in Matsui et al. (1998). In such a system, no constant pressure gradient can be present, due to the fact that the pressure must be continuously moving around the culture. It should be noted that additional local variations in pressure due to osmotic fluxes may be present, as would be predicted from the Isotonic Volume Hypothesis of Boucher (1994). For now, we shall not consider the effect of a pressure gradient, although it is possible that in vivo such an effect may be important.

4.3. Modelling an infinite metachronal array of cilia between two parallel plates

In Liron (1996), it is argued that the averaging technique of Eq. (20) is by no means accurate, since the variations of $\underline{\mathbf{S}}(\mathbf{x}, \boldsymbol{\xi}'_{m0}(s,t))$ in x_2 for $\mathbf{x}$ close to $\boldsymbol{\xi}'_{m0}(s,t)$ are significant. Liron calculated exponentially decreasing forms of the doubly-infinite sums of the Stokeslets as a remedy for this. An alternative approach is to retain the exact form of the near-field singularities and perform the averaging in the far-field only. By not averaging in the near-field, we also can check that the boundary condition discussed in Section 2.3 is satisfied by the solution. We shall work in the confined domain, using the Stokeslet $\mathbf{S}_k^C$. As before, we start with the doubly-infinite field of cilia. Assuming without loss of generality that the point $\mathbf{x}$ lies close to the cilium with base at $(m^*a, 0)$, $0 \le m^* \le m_0$, given by $\boldsymbol{\xi}'_{m^*0}(s,t)$, we add a local distribution of dipoles to represent the nearby cilium as a slender curved ellipsoid:

$$\begin{aligned}\mathbf{u}(\mathbf{x}) = &\sum_{n=-\infty}^{\infty} \sum_{m=-\infty}^{\infty} \int_0^1 f_k(\boldsymbol{\xi}'_{mn}(s^*)) \mathbf{S}_k^C(\mathbf{x}, \boldsymbol{\xi}'_{mn}(s^*))\, \mathrm{d}s^* \\ &+ \int_0^1 \frac{\alpha^2}{1/2 + 2\alpha^2} s^*(1-s^*)\, f_k(\boldsymbol{\xi}'_{m^*0}(s^*)) \mathbf{K}_k(\mathbf{x}, \boldsymbol{\xi}'_{m^*0}(s^*))\, \mathrm{d}s^*.\end{aligned} \tag{21}$$

Separating out the 'local' cilium, this can be rewritten, in the notation of Eq. (10), as

$$\mathbf{u}(\mathbf{x}) = \sum_{n=-\infty}^{\infty}\sum_{m=-\infty}^{\infty} \mathbf{I}[\mathbf{x}, \boldsymbol{\xi}'_{mn}; \underline{\mathbf{S}}^C, \mathbf{f}] - \mathbf{I}[\mathbf{x}, \boldsymbol{\xi}'_{m^*0}; \underline{\mathbf{S}}^C, \mathbf{f}] + \mathbf{I}[\mathbf{x} - ra\hat{\mathbf{x}}_1, \boldsymbol{\xi}^{m^*}; \underline{\mathbf{G}}^C, \mathbf{f}]. \tag{22}$$

Recall that the singularity $\underline{\mathbf{G}}^C$ is the Stokeslet-dipole combination of Eq. (9). Noting that the first line will not vary rapidly with x_2, we average this line in the x_2 direction as in Section 4.1,

$$\mathbf{u}(\mathbf{x}) = \frac{1}{b}\sum_{r=0}^{m_0-1} \mathbf{I}[\mathbf{x} - ra\hat{\mathbf{x}}_1, \boldsymbol{\xi}^r; \underline{\mathbf{D}}^C, \mathbf{f}] - \mathbf{I}[\mathbf{x} - m^*a\hat{\mathbf{x}}_1, \boldsymbol{\xi}^{m^*}; \overline{\underline{\mathbf{S}}}^C, \mathbf{f}] + \mathbf{I}[\mathbf{x} - m^*a\hat{\mathbf{x}}_1, \boldsymbol{\xi}^{m^*}; \underline{\mathbf{G}}^C, \mathbf{f}], \tag{23}$$

where $\overline{\underline{\mathbf{S}}}^C = (1/b)\int_{-b/2}^{b/2} \underline{\mathbf{S}}^C(\mathbf{x}, \boldsymbol{\xi})\, \mathrm{d}x_2$.

4.4. A new model for the flow in the periciliary layer

A model for cilia beating in a domain bounded by two flat plates was first proposed by Blake (1973) for approximating a ciliated tubule such as the ductus efferentes of the male reproductive tract. He suggested taking the single plate solution he had developed previously near each plate, then connecting the solution by a flat or parabolic profile. Liron and Mochon (1976b) gave the analytical solution that we denote S^C_{jk}, expressed in terms of Hankel transforms, and an alternative version in terms of exponentially decreasing series. Unfortunately, for **y** close to the walls of the domain, these forms of the solution decay quite slowly, making computation more time consuming. A remedy was provided by Staben et al. (2003) who found that the slowly-decaying parts of the integrands are given by the infinite domain Stokeslet plus the image corrections in each wall $S^{\text{wall}_i}_{jk}$ found by Blake (1971). The remaining part of the singularity is given in terms of rapidly decaying Hankel integrals on $(0, \infty)$, so that we have

$$S^C_{jk} = S^{\infty}_{jk} + S^{\text{wall}_0}_{jk} + S^{\text{wall}_1}_{jk} + S^{\text{Hankel}}_{jk}. \tag{24}$$

A very useful technical maneuver when applying the refined discretisation technique of Eq. (8) is to notice that only the first three terms may be singular near the point of evaluation and hence rapidly varying. The S^{Hankel}_{jk} term will not be rapidly varying and, hence, it is only necessary to evaluate the lengthy integrals defining S^{Hankel}_{jk} at the single point in each segment s_i. If speed of implementation is an issue, it may also be useful to exploit the analytics of Higdon (1979), who evaluated S^{∞}_{jk} in the region close to the singular point. Other analytical techniques based on regu-

larised Stokeslets have recently been used by Tornberg and Shelley (2004), for the problem of simulating multiple interacting slender bodies with coupled elasticity.

We shall use the concept of a fluid between two parallel plates to represent the PCL. The mucous boundary, which remains relatively flat and is almost solid compared to the PCL is hence modelled as a flat no-slip boundary. We argue that this is a good approximation because '... cilia encounter mucus as a solid ...' (Salathe et al., 1997) and '... the response of the mucous layer lying on top of the bed of beating cilia is that of a semi-solid sheet ...' (Meyer and Silberberg, 1980). In order to accommodate the movement of the mucous layer, we again exploit the linearity of the Stokes flow equation by adding a time-dependent shear-driven flow given by the traction layer model of Smith et al. (2006). This phenomenological model captured most of the main physical effects and interaction of the PCL and mucous layer, but did not model the detailed flow patterns around the cilia in the PCL. In order to investigate this, we combine the mucous layer movement with the cilia-induced flow to provide a higher level of detail on the flow in the PCL.

The ciliated plate, representing the epithelium, is at $x_3 = 0$, the moving plate, representing the mucous layer, is at $x_3 = L$. We split the total velocity $\mathbf{u}$ into two parts, $\mathbf{u} = \mathbf{u}^{(1)} + \mathbf{u}^{(2)}$, where $\mathbf{u}^{(1)}$ is the solution for shear–driven flow, discussed in Section 4.5.

At present, we assume that the epithelium is impermeable, corresponding to the boundary condition that $u = v = 0$ on $x_3 = 0$. This is consistent with the hypotonic defensin hypothesis discussed in Smith et al. (2006). As discussed in Section 5.2, it will be an important topic for future work to model flow produced by transepithelial fluxes. It may also be important to modify the singularities used to take into account possible slip at the epithelial surface, or even porosity of the mucous layer.

4.5. Shear-driven flow

In this section, we describe the fluid flow $\mathbf{u}^{(1)}$ that represents the effect of the mucous layer moving in contact with the PCL. The fluid is stationary at the epithelium, so that $\mathbf{u}^{(1)} = 0$ at $y = 0$. At $y = 1$, we use the velocity calculated for the traction layer numerical model in Smith et al. (2006), at the level of the mucus–PCL interface. The component of $\mathbf{u}^{(1)}$ into the paper was neglected for the 2D model traction layer model, we take it to be zero. With the above boundary conditions, we solve the Stokes equations in order to calculate the shear-driven flow $\mathbf{u}^{(1)}$. Details are given in Appendix A. The calculated velocity field $\mathbf{u}^{(1)}$ is shown as a quiver plot in Fig. 15.

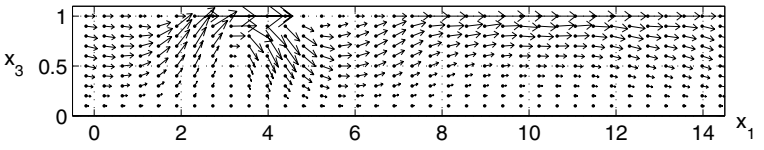


Fig. 15 Fluid velocity vectors for the shear-driven flow $\mathbf{u}^{(1)}$ only. Axes scaled with respect to cilium length L, $L = 6$ μm, wavelength $\lambda = 90$ μm.

4.6. Integral equation

Using the analysis from Section 4.3 we have

$$\mathbf{u}(\mathbf{x}) = \frac{1}{b}\sum_{r=0}^{m_0-1} \mathbf{I}[\mathbf{x} - ra\hat{\mathbf{x}}_1, \boldsymbol{\xi}^r; \underline{\mathbf{D}}^C, \mathbf{f}] - \mathbf{I}[\mathbf{x} - m^* a\hat{\mathbf{x}}_1, \boldsymbol{\xi}^{m^*}; \overline{\underline{\mathbf{S}}}^C, \mathbf{f}] + \mathbf{I}[\mathbf{x} - m^* a\hat{\mathbf{x}}_1, \boldsymbol{\xi}^{m^*}; \underline{\mathbf{G}}^C, \mathbf{f}] + \mathbf{u}^{(1)}(\mathbf{x}). \tag{25}$$

By replacing $\mathbf{x}$ with $\boldsymbol{\xi}^{m^*}(s)$ and $\mathbf{u}(\mathbf{x})$ with $\dot{\boldsymbol{\xi}}^{m^*}(s)$, we then have an integral equation for the Stokeslet strengths $\mathbf{f}^{m^*}(s)$ for $m^* = 0, \ldots, m_0 - 1$ and $0 < s < 1$, which is solved using the same discretisation as for Eq. (8). Once the force distribution is found, the fluid velocity at any position $\mathbf{x}$ may be found from Eq. (26).

4.7. Results

Figure 16 shows velocity field solutions for our model at different points along the ciliary beat at time $t = 0$, for 50 cilia per wavelength. The beat cycle quantified by Fulford and Blake (1986b), taken from the data of Sanderson and Sleigh (1981), was used. It was necessary to choose the metachronal wavelength to be $m_0 a = 15L = 90$ μm, rather longer than the value of 30 μm quoted by Fulford and Blake (1986b). This length was chosen to prevent the cilia from 'intersecting.' In the real system, the cilia would be likely to slip past each other. However, our slender body model is not designed for the situation in which the cilia approach this closely. Figure 17 shows that the boundary conditions on the cilium at the origin are approximately satisfied, although due to the greater cilium density, the results are not as accurate as the single cilium model shown in Fig. 6. The spacing between cilium centres is 1.8 μm, in the lungs the spacing will be of the order of 0.3 μm; however, our model provides an improved indication of the flows in the densely ciliated system of the airway.

Comparing the results with Fig. 15, it is notable that the cilia do not have a significant effect on the flow field except very near the cilium axis. The flow is dominated by shear-driven flow originating in the mucous layer. This is even more clear from the plot in Fig. 18.

Figure 19 shows the flow profile in the region between the cilia tips and the mucous layer. It is interesting to note that the backward movement of the cilia tips does not cause a backward flow of fluid, but rather the PCL flows forward with the mucous layer. The gap between the cilia tips and the mucus interface was not modelled in Smith et al. (2006), which predicted very small transport of PCL. Our results presented here suggest that there could be substantial transport of PCL in this gap. As for the embryonic cilia results, the velocity induced by a moving cilium decays rapidly, due to the $1/r^2$ far-fields found by Blake (1971) and Liron (1978).

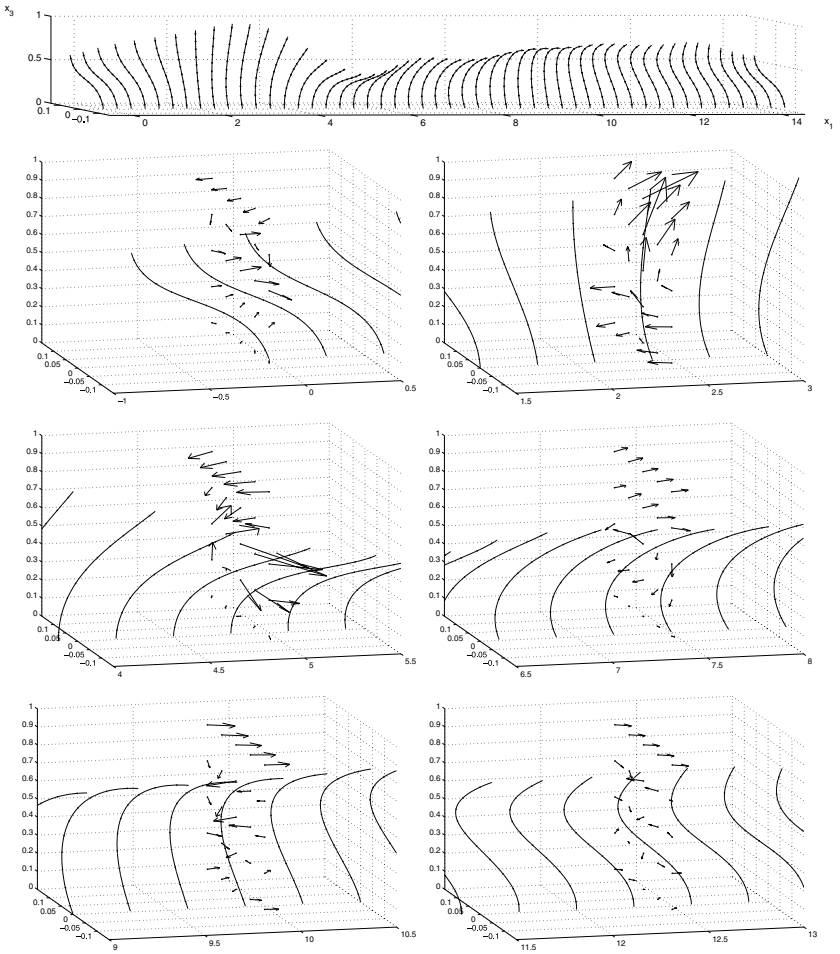


Fig. 16 *Top*—a line of cilia over one wavelength, with the beat cycle discretised by Fulford and Blake (1986b) from the micrographs of Sanderson and Sleigh (1981). *Below*—close-up plots of the fluid velocity vectors at six points along the beat cycle. The upper left and right plots show the profiles at the beginning and apex of the effective stroke. The middle left plot shows the start of the recovery stoke. The remaining plots show the rest of the recovery stoke, with the cilia reversing the direction of the flow in the region below the cilia tips, and most significantly in the region of the line of centres of the cilia. Above the cilia tips, the forward flow is maintained despite the cilia beating backwards. $m_0 = 50$ cilia, $N = 10$ nodes, $Q = 11$ refinement points. Results calculated using Eq. (26).

4.8. Discussion

In this section, we have presented a new, mathematically tractable model for the fluid flow in the PCL, based on some simplifying assumptions such as the flatness of the mucus–PCL interface, and zero flux through the epithelium. The results provide a new level of detail into the nature of the three-dimensional oscillatory

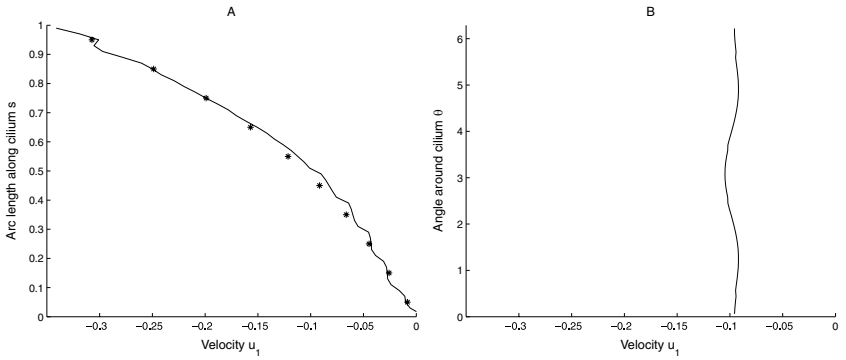


Fig. 17 Checking the boundary conditions on the cilium at the origin for the results shown in Figure 16. (A) Profile along cilium. $N = 10$, $Q = 11, \alpha = 0.1/6$. (B) Profile around cilium at $s = 0.5$. Velocity scaled with respect to σL. Results calculated using Eq. (26).

flow field. Our results are very acceptably consistent with the boundary conditions on the cilia, and include the effect of viscoelastic mucus movement, using the phenomenological modelling results of Smith et al. (2006). The fluid flow is dominated by the shear-driven flow produced by the moving mucous layer, cilia only reversing the fluid flow in a region of approximately 0.2 μm in radius, the cilium radius being 0.1 μm. Our main conclusion is that there is a significant forward flow of PCL in the gap between the cilium tips and the mucus interface. It was not possible to make definitive conclusions regarding the mean flux of PCL due to the fact that integrating the errors in the singularity distributions over the fluid volume would not be acceptably accurate. It will be necessary to carry out simulations with the cilium spacing reduced to a more biologically accurate value of as little as 0.3 μm in order to make make definitive conclusions regarding the effect of the cilia on the flow in the PCL. Improved slender body theory for the case of closely approaching cilia will be instrumental in this.

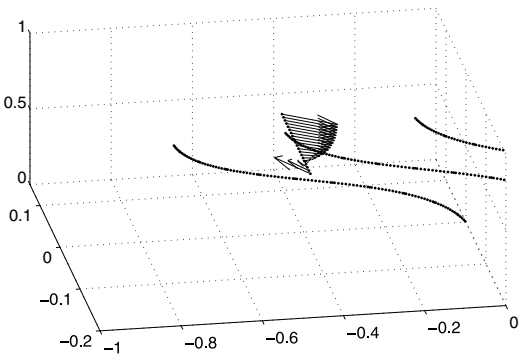


Fig. 18 Fluid velocity vectors on the line $x_1 = \xi_1(0.5, 0), 0 < x_2 < b/2, x_3 = \xi_3(0.5, 0)$ during the recovery stroke. The cilium reverses the flow in a region of radius 0.18 μm.

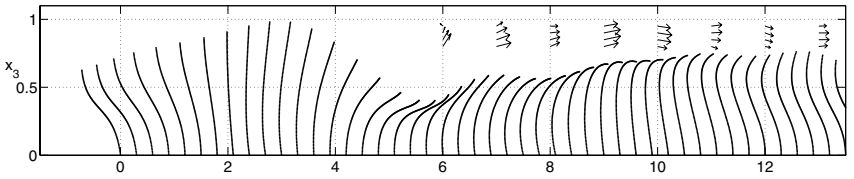


Fig. 19 Diagram showing the positive fluid transport in the region between the cilia tips and the mucous layer during the recovery stroke.

The purpose of our analysis was to retain the high efficiency of the Liron (1978) technique, while recovering near-field detail of the flow around the cilia. An alternative approach would be to use the doubly-infinite arrays of Stokeslets calculated by Liron (1996), which are in the form of exponentially decreasing doubly-infinite series. However, this would still involve a very substantial computation. In particular, the present approach allowed us to make use of the simplification of Staben et al. (2003) in the evaluation of the point force singularity.

It will be very informative to find out whether the PCL flux for a very dense mat of cilia is indeed as small as was estimated in Smith et al. (2006), although the positive flux above the cilia tips during the recovery stroke suggests that this is unlikely. In order to determine the PCL flux accurately, one could pursue an exact Boundary Integral Equation approach, or the Immersed Boundary Method that has been used successfully to model flagellar beating and cilia interaction (for a recent review, see Fauci and Dillon, 2006). Such approaches consider the cilia as elastic surfaces rather than simply one-dimensional lines. However, as discussed below, they are necessarily more computationally expensive. A study examining the flux through a small array of cilia using such techniques may be very informative.

5. Biological applications of discrete cilia modelling and the singularity technique

5.1. Scope of the singularity technique

A number of current research areas in biology require an understanding of the detailed nature of flow fields produced by, and possibly sensed by, eukaryotic cilia and flagella. Such flows may be difficult to visualise through tracer experiments due to the small length scales involved (Smith et al., 2007). By using the slender body modelling algorithms developed here, which draw on the work of Chwang and Wu (1975) and Liron (1978), it is possible to accurately represent the cilia as discrete bodies, and to simulate flow patterns produced in a Newtonian liquid by 50 or more cilia, or periodic arrays, with dominant boundary effects such as the epithelium or an upper mucous layer included in a natural way. It is also possible to perform particle tracking for time-dependent problems such as non-metachronal cilia in the embryonic node. Being able to determine the cilia-driven fluid flow in such systems as the embryonic node, or in the folds of the oviduct is crucial to biological understanding of chemical or mechanical signalling systems. For many

systems, the most crucial challenge in applying the technique in a physiologically accurate way is taking account of closely-spaced cilia.

In simulating cilia as discrete objects, the singularity method offers advantages over both local Gray & Hancock-type 'resistance coefficient' models, in that accuracy is far greater, and over highly accurate Boundary Integral Equation methods. By representing the cilia by one-dimensional line integrals, computational efficiency is greater. Boundary Integral Equation methods have greater versatility in their ability to represent non-slender and irregular boundaries, and closely spaced cilia, and Immersed Boundary Methods may be used to represent all manner of complex and realistic fluid properties. However, these techniques may still involve prohibitive computational cost when modelling large numbers of cilia, or systems where assumptions of periodicity are not possible. Extending singularity modelling to a wider class of problems is, hence, an important subject for future work. We also suggest that hybrid models that exploit the accuracy of Boundary Integral Equation methods in the near-field, together with highly efficient slender body representations for cilia in the far-field may be fruitful.

In systems such as the embryonic node, where spatially averaged 'volume force' assumptions are inappropriate, the discrete cilia technique is by far the best method of determining fluid flow. In the muco-ciliary system, such volume force models (Smith et al., 2006) are more appropriate, but discrete cilia modelling can determine subtleties that may be missing from volume force modelling, such as the positive fluid transport above the cilia tips during the recovery stroke. We strongly argue that the singularity technique is the method of choice for modelling oscillatory flow in the embryonic node. It offers both realistic physics and temporal detail in a way that is still easy to implement numerically.

Finally, it is timely and important to re-visit the mechanics of oviductal cilia, which motivated the original study of Liron (1978). A topic of considerable current interest in human and mammalian reproductive biology is the role of chemotaxis and/or thermotaxis in guiding sperm to the egg or indeed selecting sperm for fertilisation (Eisenbach and Giojalas, 2006). In vitro experiments may involve examining the response of sperm to artificial chemical or thermal gradients. However, it is not clear how such gradients relate to the in vivo situation where ciliary mixing may be important (Fauci and Dillon, 2006). For example, cilia-driven oscillations can obliterate chemical concentration gradients in airway surface liquid (Smith et al., 2007). The singularity technique may be the method of choice for calculating the oscillatory flow field. Certain difficulties arise in formulating a model: at present there do not appear to be detailed measurements of cilia density, beat pattern or metachronism at different locations along the mammalian oviduct, as exist for the lung. Towards the fimbral end of the oviduct, the geometry is rather tortuous and complex, but nearer the utero-tubular junction it is closer to a cylindrical tubule, which is closer to the problem considered by Liron (1978). Finally, ciliated cells are interspersed by mucus-secreting cells. It is, therefore, necessary to determine the rheological properties of the oviductal fluid, and whether cilia–mucus interaction takes place.

The videos of Talbot et al. (1999) show dramatically the process of cumulus–oocyte complex 'pickup' and transport by oviductal cilia. The precise mechanics of the interaction between cilia and the viscoelastic cumulus have not been

investigated. We speculate that the tips of the cilia will engage with cumulus only during the effective stroke, as for the muco-ciliary system of the lung. Hence, oviductal cilia may exhibit two very different functions—the mixing of oviductal fluid, and the directional transport of viscoelastic cumulus.

5.2. Future developments

Below we outline a number of areas in which the singularity technique may be extended to give greater insight into various biological problems.

- *Slip conditions and porous epithelia*: Future work may also consider the role of 'slip' in microfluidics, as discussed recently by Lauga et al. (2005), or even fluid boundaries such as mucus that may act as porous media. How does possible slip on a ciliated surface, or a surface near a swimming organism modify flow generation, swimming speed or efficiency? Cells possessing primary cilia are generally covered in short, dense microvilli (see, for example, the images of Hagiwara et al., 2002). A slip condition may be an appropriate boundary condition on the 'surface' of the microvilli. In the case of muco-ciliary transport in the liquid lining of the lung, the inclusion of porous medium effects to simulate epithelial permeability may assist with bringing theoretical modelling into closer correspondence with biological understanding (see, for example Matsui et al., 1998, 2000; Smith et al., 2007).
- *Closely approaching cilia*: Bartha and Liron (1988b) used the asymptotic techniques of Johnson (1980) to consider the interaction of two slender bodies either in an unbounded fluid, or near a wall. They found asymptotically accurate second-kind integral equations for the force distributions and drag on each body, subject to their separation being of the order of the cilium length. It would be very useful to determine whether such techniques could work for bodies with separation of a small multiple of their slenderness, as is likely to be the case in certain physiological systems such as the lung, oviduct and even stereocilia in the cochlea. As discussed above, a hybrid approach may be optimal.
- *Mechanosensing of slender filaments*: Gueron and Levit-Gurevich (2001) have also recently considered 3D flow due to arrays of cilia. Moreover, they have coupled modelling of the internal $9 + 2$ structure and bend generation with the fluid dynamics of the LGL Theorem discussed earlier, and the 3D kinematics of the motion of a slender filament. Their approach shows how for relatively large arrays of cilia (up to 25 were used in their study) one can investigate the emergence of ciliary coordination for three-dimensional flow. The authors noted that this has applications to a number of biological systems, to which we would like to add the investigation of the bending of mechanosensory cilia to sense fluid flow in the embryonic node. It is also possible that airway cilia transduce shear stress from airflow, which has been shown to have a very significant effect on mechanisms that control ASL depth (Tarran et al., 2006). Discrete cilia modelling could be used to quantify whether such stresses would be significant in the presence of the considerable stresses caused by nearby motile cilia, and to determine the amount of stress on the underlying epithelium.

- *Flagellar propulsion*: The singularity technique for a slender body used in this paper has much in common with the flagellar propulsion model of Higdon (1979), some important differences being that modelling free-swimming bodies involves an additional force and moment balance, and that Higdon performed an analytical integral for the singularity in the near-field. With present computational techniques, this latter maneuver is not required, and furthermore we can consider a more sophisticated singularity representation that takes into account plane boundaries and a more realistic beat of the tail. A vital future step in the modelling of sperm will be to integrate Higdon's classic framework with more accurate representations of the head and boundary geometries that motile cells encounter in vivo, and to extend these techniques to take into account the rheology of fluids such as cervical mucus. An initial study involving the latter has been done by Fulford et al. (1998).

Acknowledgments

The authors would like to thank the faculty and students at the Cystic Fibrosis/Pulmonary Research and Treatment Center and the Department of Applied Mathematics, University of North Carolina, Chapel Hill for valuable discussions regarding airway surface liquid transport. The authors would also like to thank Dr S. Nonaka of the Graduate School of Frontier Biosciences, Osaka University, Japan for valuable information regarding experiments on the embryonic node. The majority of this work was conducted while DJS was funded by an EPSRC studentship; part of this work was completed while DJS was funded by a Wellcome Trust 'Value in People' Postdoctoral Fellowship.

Appendix: Shear-driven component of the flow in the periciliary liquid

Below we describe how the shear-driven component of the flow $\mathbf{u}^{(1)}$ is derived. For simplicity, we use the notation u, v for the x_1 and x_3 components of the velocity $u_1^{(1)}$ and $u_3^{(1)}$, and x, y for x_1, x_3. Following Smith et al. (2006), we write the solution as a finite Fourier series $u = \sum_{n=0}^{15} u_n$, make the transformation $u_n = \mathrm{Rl}\{(\check{u}_n^r + \mathrm{i}\check{u}_n^i)\,\mathrm{e}^{\mathrm{i}n(kx+\sigma t)}\}$ and nondimensionalise u, v, x, y, p with scalings σL, $\sigma L^2/\lambda$, λ, L, $\mu\sigma\lambda/L$, respectively. In what follows, we omit the subscripts.

For $n = 0$ we have

$$\frac{\mathrm{d}^2 u}{\mathrm{d}y^2} = 0, \tag{A.1}$$

and for $n \geq 1$

$$-2\pi n\check{p}^i = -\chi^2\check{u}^r + \frac{\mathrm{d}^2\check{u}^r}{\mathrm{d}y^2}, \qquad 2\pi n\check{p}^r = -\chi^2\check{u}^i + \frac{\mathrm{d}^2\check{u}^i}{\mathrm{d}y},$$

$$\frac{\mathrm{d}^2\check{p}^r}{\mathrm{d}y^2} = -\chi^2\epsilon^2\check{v}^r + \epsilon^2\frac{\mathrm{d}^2\check{v}^r}{\mathrm{d}y^2}, \qquad \frac{\mathrm{d}\check{p}^i}{\mathrm{d}y} = -\chi^2\epsilon^2\check{v}^i + \epsilon^2\frac{\mathrm{d}^2\check{v}^i}{\mathrm{d}y^2}, \tag{A.2}$$

along with the differentiated continuity equations

$$-2\pi n\frac{\mathrm{d}\check{u}^i}{\mathrm{d}y} + \frac{\mathrm{d}^2\check{v}^r}{\mathrm{d}y^2} = 0, \quad 2\pi n\frac{\mathrm{d}\check{u}^r}{\mathrm{d}y} + \frac{\mathrm{d}^2\check{v}^i}{\mathrm{d}y^2} = 0, \tag{A.3}$$

where $\epsilon = L/\lambda$ and $\chi = 2\pi nL/\lambda$.

The flow is determined by the boundary conditions on $y = 0$ and $y = 1$. On $y = 0$, assuming the epithelium is impermeable, we have $u = v = 0$. On $y = 1$, we use the interface velocity calculated in Smith et al. (2006), with horizontal and vertical components $u_{\mathrm{tl}}(x,t) = \sum_{n=0}^{15} \mathrm{Rl}\{(\check{u}^r_{\mathrm{tl}\,n} + i\check{u}^i_{\mathrm{tl}\,n})\mathrm{e}^{in(kx+\sigma t)}\}$ and $v_{\mathrm{tl}}(x,t) = \sum_{n=0}^{15} \mathrm{Rl}\{(\check{v}^r_{\mathrm{tl}\,n} + i\check{v}^i_{\mathrm{tl}\,n})\,\mathrm{e}^{in(kx+\sigma t)}\}$.

For $n = 0$, assuming no steady pressure gradient as in Smith et al. (2006), we have the shear-driven flow solution

$$u(y) = u_{\mathrm{tl}\,0}\frac{y}{L}. \tag{A.4}$$

For $n \geq 1$, we rewrite this as a system of 10 first-order ODEs—from the six equations above and four definition equations—in 10 variables. Primes denote differentiation with respect to y.

$$\begin{array}{ll} Z_1 = \check{u}^r & Z_6 = \check{p}^i \\ Z_2 = \check{u}^i & Z_7 = -2\pi n\check{u}^i + \check{v}^{r\prime} \\ Z_3 = \check{v}^r & Z_8 = -2\pi n\check{u}^i + \check{v}^{r\prime} \\ Z_4 = \check{v}^i & Z_9 = \check{u}^{r\prime} \\ Z_5 = \check{p}^{r\prime} & Z_{10} = \check{u}^{i\prime}. \end{array}$$

The field equations are then written as

$$\begin{array}{ll} Z'_1 = Z_9 & Z'_6 = -\chi^2\epsilon^2 Z_4 - 2\pi n\epsilon^2 Z_9 \\ Z'_2 = Z_{10} & Z'_7 = 0 \\ Z'_3 = 2\pi n Z_2 + Z_7 & Z'_8 = 0 \\ Z'_4 = -2\pi n Z_1 + Z_8 & Z'_9 = \chi^2 Z_1 - 2\pi n Z_6 \\ Z'_5 = -\chi^2\epsilon^2 Z_3 + 2\pi n\epsilon^2 Z_{10} & Z'_{10} = \chi^2 Z_2 + 2\pi n Z_5. \end{array}$$

The boundary conditions are written as

$$\begin{array}{lll} & & Z_1 = 0 \\ Z_1 = \check{u}^r_{\mathrm{tl}\,n} & & Z_2 = 0 \\ Z_2 = \check{u}^i_{\mathrm{tl}\,n} & & Z_3 = 0 \\ Z_3 = \check{v}^r_{\mathrm{tl}\,n} & & Z_4 = 0 \\ Z_4 = \check{v}^i_{\mathrm{tl}\,n} & (y = 1), & Z_7 = -2\pi n\check{u}^i + \check{v}^{r\prime} \\ & & Z_8 = -2\pi n\check{u}^i + \check{v}^{r\prime} \quad (y = 0). \end{array}$$

This system is solved numerically using the NAG routine D02GBF.

References

Bartha, E., Liron, N., 1988a. Slender body interactions for low Reynolds numbers. Part 1. Body–wall interactions. SIAM J. Appl. Math. 48, 992–1008.

Bartha, E., Liron, N., 1988b. Slender body interactions for low Reynolds numbers. Part 2. Body–body interactions. SIAM J. Appl. Math. 48, 1262–1280.

Batchelor, G.K., 1970. Slender-body theory for particles of arbitrary cross-section in Stokes flow. J. Fluid Mech. 44, 419–440.

Blake, J.R., 1971. A note on the image system for a Stokeslet in a no slip boundary. Proc. Camb. Phil. Soc. 70, 303–310.

Blake, J.R., 1972. A model for the micro-structure in ciliated organisms. J. Fluid Mech. 55, 1–23.

Blake, J.R., 1973. Mucus flows. Math. Biosci. 17, 301–313.

Blake, J.R., Chwang, A.T., 1974. Fundamental singularities of viscous flow. Part 1. Image systems in the vicinity of a stationary no-slip boundary. J. Eng. Math. 8, 23–29.

Blake, J.R., Sleigh, M.A., 1974. Mechanics of ciliary locomotion. Biol. Rev. Camb. Philos. Soc. 49(1), 85–125.

Boucher, R.C., 1994. Human airway ion transport. Part 1. Am. J. Respir. Crit. Care Med. 150, 271–281.

Brokaw, C.J., 2005. Computer simulation of flagellar movement IX. Oscillation and symmetry breaking in a model for short flagella and nodal cilia. Cell Motil. Cytoskeleton 60, 35–47.

Brown, N.A., Wolpert, L., 1990. The development of handedness in left/right asymmetry. Development 109, 1–9.

Buceta, J., Ibañes, M., Rasskin-Gutman, D., Okada, Y., Nobutaka, N., Izpisúa-Belmonte, J.C., 2005. Nodal cilia dynamics and the specification of the left/right axis in early vertebrate embryo development. Biophys. J. 89, 2199–2209.

Burgers, J.M., 1938. On the motion of small particles of elongated form suspended in a viscous liquid. Kon. Ned. Akad. Wet. Verhand. (Eerste Sectie) 16, 113.

Cartwright, J.H.E., Piro, O., Tuval, I., 2004. Fluid-dynamical basis of the embryonic development of left–right asymmetry in vertebrates. Proc. Natl. Acad. Sci. U.S.A. 101 (19), 7234–7239.

Childress, S., 1981. Mechanics of Swimming and Flying. Cambridge University Press, New York.

Chwang, A.T., Wu, T.Y., 1975. Hydrodynamics of the low-Reynolds number flows. Part 2. The singularity method for Stokes flows. J. Fluid Mech. 67, 787–815.

Clarke, R.J., Jensen, O.E., Billingham, J., Williams, P.M., 2006. Three-dimensional flow due to a microcantilever oscillating near a wall: An unsteady slender-body analysis. Proc. R. Soc. A 462, 913–933.

Cox, R.G., 1970. The motion of long slender bodies in a viscous fluid. Part 1. General theory. J. Fluid Mech. 44, 791–810.

Eisenbach, M., Giojalas, L.C., 2006. Sperm guidance in mammals—an unpaved road to the egg. Nat. Rev. Mol. Cell Biol. 7, 276–285.

Fauci, L., Dillon, R., 2006. Biofluidmechanics of reproduction. Ann. Rev. Fluid Mech. 38(1), 371–394.

Fulford, G.R., Blake, J.R., 1986a. Force distribution along a slender body straddling an interface. J. Aust. Math. Soc., Ser. B, Appl. Math. 27(3), 295–315.

Fulford, G.R., Blake, J.R., 1986b. Muco-ciliary transport in the lung. J. Theor. Biol. 121, 381–402.

Fulford, G.R., Katz, D.F., Powell, R.L., 1998. Swimming of spermatozoa in a linear viscoelastic fluid. Biorheology 35(4–5), 295–309.

Gueron, S., Levit-Gurevich, K., 2001. A three-dimensional model for ciliary motion based on the internal $9 + 2$ structure. Proc. R. Soc. Lond. B 268, 599–607.

Gueron, S., Liron, N., 1992. Ciliary motion modeling, and dynamic multicilia interactions. Biophys. J. 63, 1045–1058.

Gueron, S., Liron, N., 1993. Simulations of three-dimensional ciliary beats and cilia interactions. Biophys. J. 65, 499–507.

Hagiwara, H., Harada, S., Maeda, S., Aoki, T., Ohwada, N., Takata, K., 2002. Ultrastructural and immunohistochemical study of the basal apparatus of solitary cilia in the human oviduct epithelium. J. Anat. 200, 89.

Hancock, G.J., 1953. The self-propulsion of microscopic organisms through liquids. Proc. R. Soc. B. 217, 96–121.
Higdon, J.J.L., 1979. A hydrodynamic analysis of flagellar propulsion. J. Fluid Mech. 90, 685–711.
Johnson, R.E., 1980. An improved slender-body theory for Stokes flow. J. Fluid Mech. 99(2), 411–431.
Kosaki, K., Casey, B., 1998. Genetics of human left–right axis malformations. Semin. Cell Dev. Biol. 9(1), 89–99.
Lauga, E., Brenner, M.P., Stone, H.A., 2005. Microfluidics: The no-slip boundary condition. In: Foss, J., Tropea, C., Yarin, A. (Eds.), Handbook of Experimental Fluid Dynamics. Springer, New York.
Lighthill, M.J., 1976. Flagellar hydrodynamics. The Jon von Neumann lecture. SIAM Rev. 18(2), 161–230.
Liron, N., 1978. Fluid transport by cilia between parallel plates. J. Fluid Mech. 86(4), 705–726.
Liron, N., 1996. Stokes flow due to infinite arrays of Stokeslets in three dimensions. J. Eng. Math. 30(1–2), 267–297.
Liron, N., 2001. The LGL (Lighthill–Gueron–Liron) Theorem–historical perspective and critique. Math. Methods Appl. Sci. 24, 1533–1540.
Liron, N., Mochon, S., 1976a. The discrete-cilia approach to propulsion of ciliated micro-organisms. J. Fluid Mech. 75, 593–607.
Liron, N., Mochon, S., 1976b. Stokes flow for a stokeslet between two parallel flat plates. J. Eng. Math. 10, 287–303.
Matsui, H., Davis, C.W., Tarran, R., Boucher, R.C., 2000. Osmotic water permeabilities of cultured, well-differentiated normal & cystic fibrosis airway epithelia. J. Clin. Invest. 105 (10), 1419–1427.
Matsui, H., Randell, S.H., Peretti, S.W., Davis, C.W., Boucher, R.C., 1998. Coordinated clearance of periciliary liquid and mucus from airway surfaces. J. Clin. Invest. 102(6), 1125–1131.
McGrath, J., Somlo, S., Makova, S., Tian, X., Brueckner, M., 2003. Two populations of node monocilia initiate left–right asymmetry in the mouse. Cell 114, 61–73.
Meyer, F.A., Silberberg, A., 1980. The rheology and molecular organization of epithelial mucus. Biorheology 17, 163–168.
Nonaka, S., Shiratori, H., Saijoh, Y., Hamada, H., 2002. Determination of left–right patterning of the mouse embryo by artificial nodal flow. Nature 418, 96–98.
Nonaka, S., Tanaka, Y., Okada, Y., Takeda, S., Harada, A., Kanai, Y., Kido, M., Hirokawa, N., 1998. Randomization of left–right asymmetry due to loss of nodal cilia generating leftward flow of extraembryonic fluid in mice lacking KIF3B motor protein. Cell 95, 829–837.
Nonaka, S., Yoshiba, S., Watanabe, D., Ikeuchi, S., Goto, T., Marshall, W.F., Hamada, H., 2005. De novo formation of left–right asymmetry by posterior tilt of nodal cilia. PLoS Biol. 3 (8), e268.
Okada, Y., Takeda, S., Tanaka, Y., Izpisúa Belmonte, J.-C., Hirokawa, N., 2005. Mechanism of nodal flow: A conserved symmetry breaking event in left–right axis determination. Cell 121, 633–644.
Orme, B.A.A., Otto, S.R., Blake, J.R., 2001. Enhanced efficiency of feeding and mixing due to chaotic flow patterns around choanoflagellates. Math. Med. Biol. 18 (3), 293–325.
Phan-Thien, N., Tran-Cong, T., Ramia, M., 1987. A boundary-element analysis of flagellar propulsion. J. Fluid Mech. 185, 533–549.
Salathe, M., O'Riordan, T.G., Wanner, A., 1997. Mucociliary clearance. In: Crystal, R.G., West, P.J., Barnes, P.J., Weibel, E.R. (Eds.), The Lung: Scientific Foundations. Lippincott–Raven, Philadelphia, pp. 2295–2308.
Sanderson, M.J., Sleigh, M.A., 1981. Ciliary activity of cultured rabbit tracheal epithelium: Beat pattern and metachrony. J. Cell Sci. 47, 331–341.
Smith, D.J., Gaffney, E.A., Blake, J.R., 2006. A viscoelastic traction layer model of muco-ciliary transport. Bull. Math. Biol. 69(1), 289–327.
Smith, D.J., Gaffney, E.A., Blake, J.R., 2007. A model of tracer transport in airway surface liquid. Bull. Math. Biol. 69(3), 817–836.
Staben, M.E., Zinchenko, A.Z., Davis, R.H., 2003. Motion of a particle between two plane parallel walls in low-Reynolds-number Poiseuille flow. Phys. Fluids 15(6), 1711–1733.
Tabin, C.J., Vogan, K.J., 2003. A two-cilia model for vertebrate left–right axis specification. Genes Dev. 17, 1–6.

Talbot, P., Geiske, C., Knoll, M., 1999. Oocyte pickup by the mammalian oviduct. Mol. Biol. Cell 10(1), 5–8.
Tang, X.Z., Boozer, A.H., 1996. Finite time Lyapunov exponent and advection–diffusion equation. Physica D 95, 283–305.
Tarran, R., Button, B., Boucher, R.C., 2006. Regulation of normal and cystic fibrosis airway surface liquid volume by phasic shear stress. Annu. Rev. Physiol. 68, 543–561.
Tillett, J.P.K., 1970. Axial and transverse stokes flow past slender axisymmetric bodies. J. Fluid Mech. 44, 401–417.
Tornberg, A.-K., Shelley, M.J., 2004. Simulating the dynamics and interactions of flexible fibers in Stokes flows. J. Comput. Phys. 196, 8–40.
Tuck, E.O., 1964. Some methods for flows past slender bodies. J. Fluid Mech. 18, 619.
Williams, W.E., 1966. Boundary effects in Stokes flow. J. Fluid Mech. 24(2), 285–291.